Tectonophysics 708 (2017) 1–14

Contents lists available at ScienceDirect

Tectonophysics

journal homepage: www.elsevier.com/locate/tecto

Cyclical shear fracture and viscous flow during transitional ductile-brittle deformation in the Saddlebag Lake Shear Zone, California

Katharine E. Compton [a], James D. Kirkpatrick [b,*], Gregory J. Holk [c]

[a] Department of Geosciences, Colorado State University, 1482 Campus Delivery, Fort Collins, CO 80523, USA
[b] Department of Earth and Planetary Sciences, McGill University, 3450 University St., Montréal, QC H3A 0E8, Canada
[c] Department of Geological Sciences, California State University, 1250 Bellflower Blvd., Long Beach, CA 90840, USA

ARTICLE INFO

Article history:
Received 19 August 2016
Received in revised form 18 March 2017
Accepted 6 April 2017
Available online 7 April 2017

Keywords:
Shear zone
Vein
Fracture
Oxygen isotope
Rheology
Tectonic tremor

ABSTRACT

Exhumed shear zones often contain folded and/or dynamically recrystallized structures, such as veins and pseudotachylytes, which record broadly contemporaneous brittle and ductile deformation. Here, we investigate veins within the Saddlebag Lake Shear Zone, central Sierra Nevada, California, to constrain the conditions and processes that caused fractures to form during ductile deformation. The shear zone mylonites contain compositional banding at centimeter- to meter- scales, and a ubiquitous, grain-scale, continuous- to spaced-foliation defined by aligned muscovite and chlorite grains. Veins of multiple compositions formed in two predominant sets: sub-parallel to the foliation and at high angle to the foliation. Some foliation sub-parallel veins show apparent shear offset consistent with the overall kinematics of the shear zone. These veins are folded with the foliation and are commonly boudinaged, showing they were rigid inclusions after formation. Quartz microstructures and fluid inclusion thermobarometry measurements indicate the veins formed by fracture at temperatures between ~400–600 °C. Quartz, feldspar and tourmaline $\delta^{18}O$ values (+2.5 to +16.5) suggest extended fluid-rock interaction that involved magmatic, metamorphic, and meteoric-hydrothermal fluids. The orientation and spatial distribution of the veins shows that shear fractures formed along mechanically weak foliation planes. We infer fracture was promoted by perturbations to the strain rate and/or pore pressure during frictional-viscous deformation in a low effective stress environment. Evidence for repeated fracture and subsequent flow suggest both the stress and pore pressure varied, and that the tendency to fracture was controlled by the rates of pore pressure recovery, facilitated by fracture cementation. The tectonic setting and inferred phenomenological behavior were similar to intra-continental transform faults that host triggered tectonic tremor, suggesting the mechanisms that caused brittle fracture during viscous deformation may be important for comparable active systems.

1. Introduction

Hydrothermal veins are commonly found within ductile shear zones that deformed predominantly by crystal-plastic deformation mechanisms (e.g. McCaig, 1988; Cartwright and Buick, 1999). They form as brittle fractures that subsequently fill with minerals deposited from long-distance, channelized fluid flow (e.g. Sibson et al., 1975; McCaig and Knipe, 1990), or sourced by local diffusion from the wall rock (Fisher and Brantley, 1992). The dependence of fracture mode and attitude on the material properties of the host rock and orientation of the stress field at the time of formation means kinematic information from veins can be used to infer the paleo-stress field orientation, particularly where evidence shows veins formed by mode I fractures (Secor, 1965; Kerrich and Allison, 1978; Ramsay, 1980; Kerrich, 1986). Veins are therefore rich in information regarding the conditions of deformation (e.g. Bons et al., 2012). Other brittle structures recognized within crystal plastic shear zones include pseudotachylytes (e.g. Passchier, 1982; Hobbs et al., 1986; Price et al., 2012; Kirkpatrick and Rowe, 2013) and cataclastic fault rocks that both result from fracturing and frictional sliding (Melosh et al., 2014).

Folded and/or dynamically recrystallized veins or pseudotachylytes potentially record cyclical, or contemporaneous on geologic time scales, brittle and ductile deformation within shear zones. In these cases, the fractures recorded by the veins, surrounded by ductiley deformed mylonites, represent deformation characterized by a transient rheology. At greenschist- to amphibolite-facies conditions, the ambient temperatures are high enough that deformation by crystal plastic mechanisms occurs at lower differential stress than fracture and frictional sliding for some mineral phases (e.g. Brace and Kohlstedt, 1980). Fractures that form in the same phase of deformation as ductile deformation therefore suggest that some factor controlling the deformation, such as the deviatoric stress, strain rate or pore fluid pressure, was perturbed to cause a change in deformation mechanism. Fracture coupled to

* Corresponding author.
E-mail address: james.kirkpatrick@mcgill.ca (J.D. Kirkpatrick).

http://dx.doi.org/10.1016/j.tecto.2017.04.006
0040-1951/

ductile deformation has been proposed to result from both local (Hobbs et al., 1986) and regional (Lavier et al., 2013) perturbations to a steady state viscously deforming system. Earthquakes at the base of the seismogenic zone that propagate to deeper levels also represent fracture (e.g. Sibson, 1980; Lin et al., 2005), and drive fluid flow (McCaig et al., 1990) at the deep extension of faults. The resulting vein compositions, attitudes and kinematics should be useful for investigating these processes.

Recent seismological observations of tectonic tremor beneath the seismogenic zone of some continental transform faults and subduction zones have renewed interest in deformation involving both fracture and aseismic slip in regimes transitional between seismic and aseismic deformation. Tectonic tremor bursts are low-amplitude, long-duration seismic signals that are distinct from earthquakes because they typically do not contain impulsive waveforms (Obara, 2002; Rubinstein et al., 2010). They are thought to represent swarms of low- and very low-frequency earthquakes (LFEs and VLFEs respectively) that are the result of shear failure on faults (Shelly et al., 2007; La Rocca et al., 2009; Shelly, 2015). Receiver functions and tomographic models suggest that tectonic tremor spatially coincides with regions of elevated pore fluid pressure (Audet et al., 2009; Wech et al., 2012). In some cases, tremor is dynamically triggered by teleseismic waves or tidal stresses, consistent with extremely low effective stresses in the source region (Rubinstein et al., 2007; Thomas et al., 2009; Houston, 2015). Because tremor hypocenters are often relatively deep (e.g. ~15–40 km on the San Andreas fault; Shelly and Hardebeck, 2010), and the inferred temperatures in transitional regions are often high (~350–1000 °C on the San Andreas Fault; Williams et al., 2004), the deformation mechanisms that drive shear failure in otherwise aseismic regions remain enigmatic. Ancient subduction zones have been shown to contain veins or mineralized shear fractures that could represent individual LFEs (e.g. Fagereng et al., 2011, 2014; Hayman and Lavier, 2014), but few constraints are available on the structures associated with triggered tremor on intra-continental faults.

In this study, we investigate veins that formed within the Saddlebag Lake segment of the Sierra Crest Shear Zone (Cao et al., 2015), central Sierra Nevada, California, to constrain the conditions that promoted fracture in a plastically deforming system. The Saddlebag Lake Shear Zone was an active structure during Cretaceous arc magmatism, and deformed at elevated temperature due to intrusion of the plutons of the adjacent Sierra Nevada batholith. We recognized quartz and feldspar veins with shear offsets that formed sub-parallel to mylonitic foliations the shear zone rocks. As these structures record shear failure in the presence of fluids they represent a failure mechanism relevant to regimes transitional between ductile and brittle deformation. The Saddlebag Lake Shear Zone was not part of a plate boundary, but triggered tremor has recently been reported from faults within the active continental arc in Japan (e.g. Chao and Obara, 2016), and it may therefore represent a useful analog. We use field and microstructural observations and stable isotope measurements from the veins to constrain the conditions that caused fracture in the ductile regime.

2. Tectonic setting

The study area is located in the central Sierra Nevada, California, north of Tioga Pass, Yosemite National Park. We focused on the Saddlebag Lake Shear Zone (SLSZ), a segment of the Late Cretaceous Sierra Crest Shear Zone, which is exposed near Saddlebag Lake (Greene and Schweickert, 1995; Tobisch et al., 1995; Tikoff and Greene, 1997; Cao et al., 2015). The Sierra Crest Shear Zone is a dextral-oblique structure that is composed of a series of segments that can be traced along strike for ~150 km in the eastern central Sierra Nevada (Fig. 1; Greene and Schweickert, 1995; Tikoff and Greene, 1997; Cao et al., 2015). Dextral deformation likely resulted from the partitioning of the oblique convergence between the Farallon and North American plates (Tobisch et al., 1995; Tikoff and de Saint Blanquat, 1997; Cao et al., 2015). Piercing

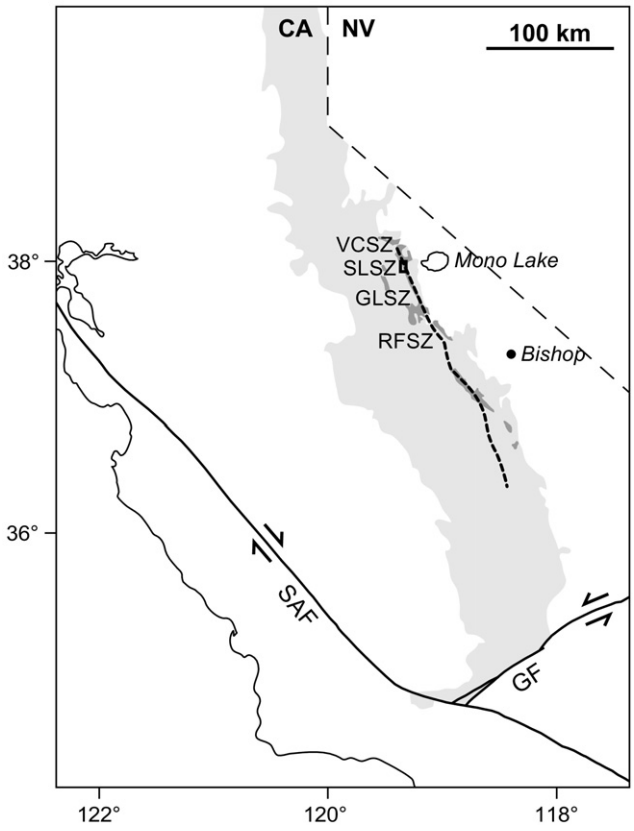

Fig. 1. Map of the Sierra Nevada batholith in California (light grey) showing locations of the eastern Sierra roof pendants (dark grey) and the Sierra Crest Shear Zone (heavy dashed line). Labeled segments of the Sierra Crest Shear Zone are the Virginia Canyon Shear Zone (VCSZ), Saddlebag Lake Shear Zone (SLSZ), Gem Lake Shear Zone (GLSZ), and Rosy Finch Shear Zone (RFSZ). San Andreas Fault (SAF) and Garlock Fault (GF) shown for reference. Location of Fig. 2 shown by the box adjacent to the SLSZ label (modified from Cao et al., 2015).

points across the Sierra Crest Shear Zone are rare, but the total dextral displacement is estimated to be several tens of kilometers (e.g. Tikoff and Teyssier, 1992; Greene and Schweickert, 1995).

The SLZS is defined by a zone of high strain in the metamorphic rocks of the Saddlebag Lake Roof Pendant and the adjacent Cretaceous plutons of the Tuolumne Intrusive Suite (Fig. 2; Cao et al., 2015). Similar to other roof pendants in the central Sierra Nevada, the Saddlebag pendant contains Paleozoic to Mesozoic units, which have all been metamorphosed to greenschist to amphibolite facies and affected by multiple orogenic events during the complex tectonic history of the western North American margin in the Phanerozoic (Brook, 1977; Albertz, 2006; Schweickert and Lahren, 2006). The pendant units are steeply dipping, generally young to the west, contain a northwest-trending cleavage, and outcrop-scale folds interpreted to have formed during the Late Jurassic Nevadan orogeny and possibly also Triassic or Cretaceous deformation events (e.g. Brook, 1977; Nokleberg and Kistler, 1980; Schweickert and Lahren, 1987).

Paleozoic miogeoclinal sedimentary units in the Saddlebag pendant consist of metamorphosed chert, conglomerate and basalts, which were faulted, folded, and metamorphosed by the Antler and Sonoma orogenies (Schweickert and Lahren, 1987). A regionally extensive, faulted unconformity defines the boundary between the Paleozoic and Mesozoic strata (Schweickert and Lahren, 1987; Stevens and Greene, 1999; Cao et al., 2015). Triassic units in the Saddlebag pendant include sequences of rhyolite, dacite, and andesite, including one ~1500 m-thick andesite package (Fig. 2; Schweickert and Lahren, 1987). Triassic metavolcanic rocks are overlain by Jurassic metasedimentary rocks, informally referred to as the Jurassic Sawmill Canyon Sequence (Schweickert and

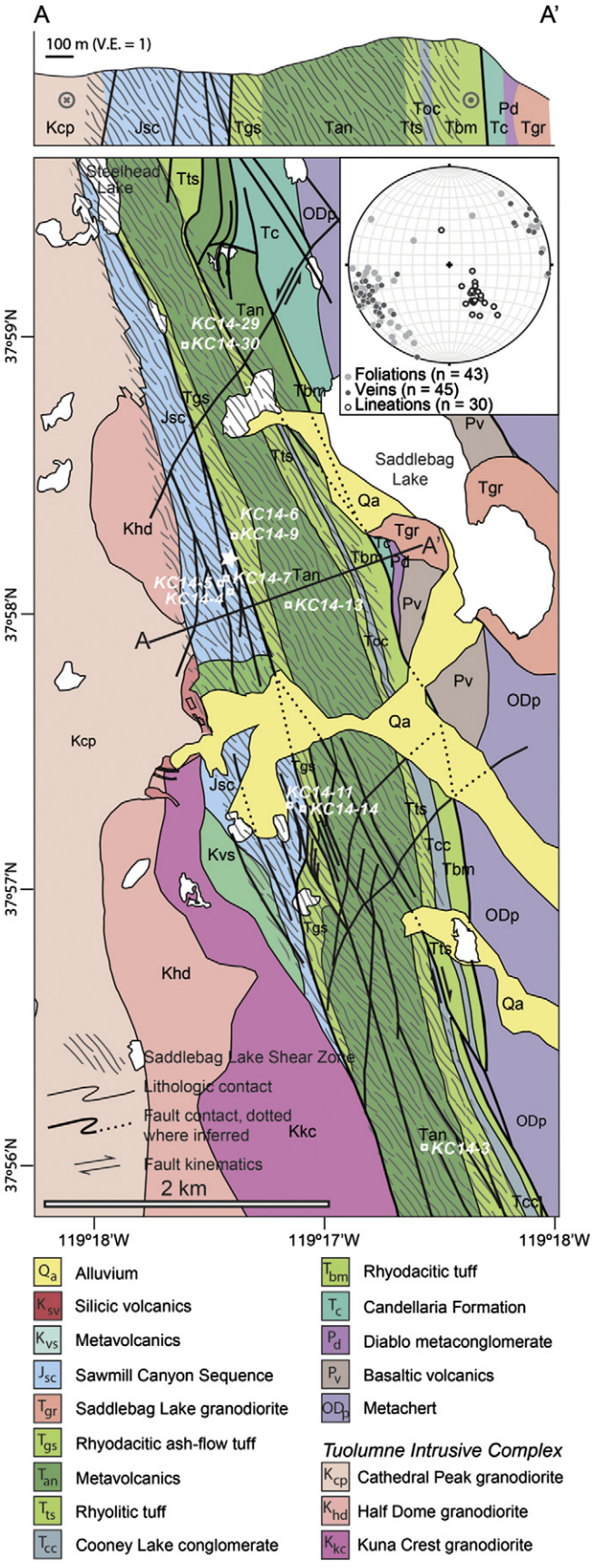

Lahren, 2006). The Sawmill Canyon Sequence is composed of cross-bedded quartzite, phyllite, and calc-silicate with local limestone, conglomerate, volcaniclastic rocks and schists (Cao et al., 2015). Cretaceous rocks in the Saddlebag Lake pendant are limited to a package of siliceous metavolcanics near the pluton boundary (Fig. 2).

The Tuolumne Intrusive Complex (TIC) is a composite arc magmatic complex that intruded the roof pendant units during the Cretaceous. Intrusive units within the TIC are ~86–94 Ma (Paterson et al., 2008; Paterson et al., 2014) and were emplaced at >700 °C and 6–10 km depth (Ague and Brimhall, 1988; Paterson et al., 2014). Pluton emplacement and cooling caused the adjacent roof pendant units to experience contact metamorphic temperatures ~700 °C to <150 °C (Kerrick, 1970; Paterson et al., 2008) and temporally and spatially variable post-intrusion cooling (Paterson and Tobisch, 1992).

The Cretaceous SLSZ is well developed along the eastern margin of the TIC (Fig. 2). The shear zone trends NNW and has been mapped over ~30 km along strike (Cao et al., 2015). The total displacement is poorly constrained, with an upper bound of tens of kilometers based on evidence from the adjacent segments of the Sierra Crest system to the south (Tikoff and Teyssier, 1992; Greene and Schweickert, 1995). The SLSZ overprinted the regional metamorphic structures. In the Saddlebag Lake area, the SLSZ deformed both the pendant units and the eastern margin of the TIC. Dikes sourced from the TIC are folded, but some crosscut the shear zone structures indicating the deformation occurred during pluton emplacement. A phase of predominantly strike-slip brittle deformation structures crosscut the shear zone (Hartman et al., 2013; Paterson and Memeti, 2014), postdating the syn-ductile deformation veins and fractures which are the focus of this study. The transition from predominantly plastic deformation to brittle deformation was caused by cooling of the TIC (Cao et al., 2015; Hartman et al., 2015). In some portions of the brittle faults, large (~10 m thick) quartz veins are present along the fault trace. Abundant chlorite- and epidote-filled fractures splay from the strike-slip faults and cut the shear zone rocks.

3. Field and microstructural observations

Key exposures within the SLSZ were selected for detailed study within a 1 km-wide area extending ~2 km along strike of the shear zone to the west and south of Saddlebag Lake where multiple sets of crosscutting veins, foliations, and fractures were visible (Fig. 2). Vein crosscutting relations and shapes in these exposures were used to infer the chronology of deformation, and sampled to determine the conditions under which structures formed from microstructural and compositional information. Horizontally rectified photographs of the exposures were generated with the Structure-from-Motion method using Agisoft's PhotoscanPro (following Johnson et al., 2014). The rectified images were used as basemaps for annotation in the field. Absolute positions and a physical scale for the images were measured with a real-time kinematic (RTK) differential GPS (accurate to ±2–3 mm).

3.1. The Saddlebag Lake Shear Zone

The Saddlebag Lake Shear Zone is defined by the presence of mylonites, isoclinal folds, a steeply dipping foliation, and steeply plunging lineation, which overprint earlier metamorphic fabrics (Fig. 3). Fold vergence, S-C structures in mylonites, asymmetric clasts in volcanic rocks, and sigma porphyroclasts that are prevalent at the millimeter-scale all indicate apparent dextral shear in sub-horizontal exposures. Asymmetric clasts in sub-vertical exposures indicate west side-up

Fig. 2. Geologic map and cross section of the study area showing the main lithologic units, the extent of the high strain Saddlebag Lake Shear Zone (SLSZ), and brittle faults (modified from Hartman et al., 2013, 2015). Foliation sub-parallel veins that were sampled for stable isotope analyses shown with white squares. The location of Fig. 9 is shown with a white star. Inset stereonet shows poles to foliation, poles to foliation sub-parallel quartz veins, and the attitudes of stretching lineations in the Jurassic and Triassic metamorphic rocks.

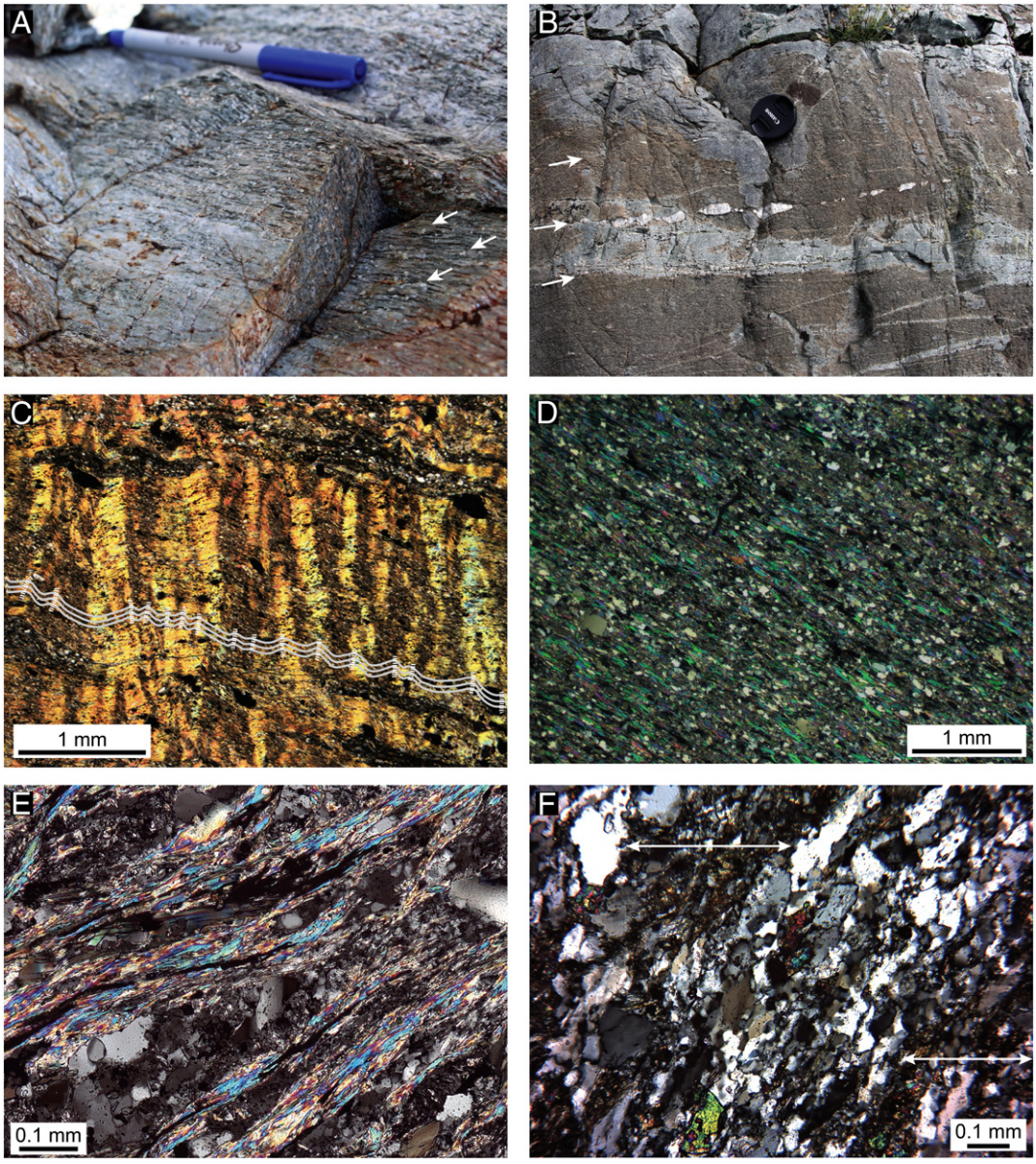

Fig. 3. A.) Photograph of mylonite within the SLSZ, approximately 250 m east of the edge of the TIC. Quartz ribbons and aligned biotite define the foliation in between rounded plagioclase porphyroclasts (arrows). Tip of the pen for scale points toward NNW. B.) Photograph of foliation sub-parallel, boudinaged quartz veins in the Jurassic silicic subunit (white arrows). Note the light-colored horizontal band in the middle of the image is due to weathering. View toward the ENE. C.) Photomicrograph of crenulation cleavage in the Triassic metavolcanics. Compositional banding that defines the early fold axes (grey lines) is gently folded (axial surfaces of later folds indicated by dashed lines). D.) Photomicrograph showing the continuous foliation in the Jurassic metasedimentary silicate subunit. Aligned muscovite grains with elongated quartz grains between them define a grain shape fabric. E.) Photomicrograph showing a more muscovite-rich sample of the Jurassic silicate subunit that contains interconnected muscovite grains in a set of anastomosing bands defining a spaced foliation. F.) Photomicrograph of the Jurassic calcsilicate unit showing foliation defined by epidote-rich bands (white arrow) with epidote-poor layers between. Note the absence of muscovite compared to D and E. All photomicrographs in cross-polarized light.

shear. Aligned chlorite and muscovite grains mostly define the foliation, but compositional banding at millimeter- to meter-scales is also common. Foliation attitudes vary slightly throughout the shear zone, ranging in strike from 294 to 358° and dip from 46 to 88°, predominantly to the northeast (Fig. 2). Bedding is isoclinally folded and transposed, and folded veins typically have axial surfaces parallel to the foliation. Veins oriented parallel to the foliation are also frequently boudinaged (Fig. 3B). A penetrative mineral lineation defined by aligned elongate crystals and grain aggregates of chlorite, quartz and/or diopside, depending on the rock type, plunges moderately to steeply (on average 55°) to the southeast. Overall, the kinematic indicators record oblique dextral, potentially transpressional, deformation with shear parallel to the lineation, consistent with other segments of the Sierra Crest Shear Zone (Tikoff and Greene, 1997; Horsman et al., 2008; Cao et al., 2015).

Mylonites within the shear zone vary from completely recrystallized rocks to rocks that deformed by crystal plastic mechanisms, but which still retain evidence for compositional banding from the protolith (Fig. 3A). The most deformed rocks occur within ~400 m of the pluton boundary. Units up to 1.5 km from the pluton boundary contain ductile deformation structures such as folds, foliations, and the mineral lineation. Further than 1.5 km from the pluton the rocks contain only the pre-Cretaceous, regionally expressed NW-trending cleavage (Schweickert and Lahren, 2006).

The shear zone deformed several of the Mesozoic units in the Saddlebag Lake pendant (Fig. 2). The Triassic metavolcanic units are very fine-grained (average grain size < 0.05 mm), and are composed of quartz, plagioclase, chlorite, and muscovite with minor rutile and hornblende. Most feldspar phenocrysts have been replaced by sericite.

Quartz phenocrysts exhibit undulose extinction and irregular grain shapes caused by dynamic recrystallization. A continuous foliation is defined by the preferred orientation of spaced muscovite and chlorite grains or by bands of fine-grained sericitized feldspar grains. Crenulation cleavage is visible in some muscovite and chlorite- and biotitite-rich interlayers near the pluton boundary (Fig. 3C).

The Jurassic metasedimentary rocks are most commonly adjacent to the TIC margin in our study area (Fig. 2), and contain abundant veins. Consequently, the majority of our observations of veins in the shear zone come from these units. The Jurassic unit can be divided into silicate and calcsilicate subunits, which are interlayered at ~10 m scales. The silicate subunit contains a fine-grained (~0.1 mm), equigranular groundmass of quartz and plagioclase (Fig. 3D). Quartz displays sweeping undulose extinction, sutured grain boundaries, and subgrain development that varies from minor to completely recrystallized. Some quartz grain boundaries form dragging structures where pinned by muscovite. Feldspars exhibit sweeping undulose extinction, but subgrain formation is rare. Aligned muscovite and chlorite grains of approximately equal size to the quartz grains are interspersed throughout the silicate subunit and are parallel to minor compositional banding at cm-scale, defining a continuous foliation (Fig. 3D). Some larger chlorite grains exhibit a platy cleavage. Variations in the chlorite and muscovite abundance define the minor compositional changes within this subunit. Where the abundance of muscovite and chlorite is higher, phyllosilicates are interconnected in anastomosing bands in which the grains (0.01 to >0.1 mm) are aligned, defining a spaced foliation (Fig. 3E). Anastomosing bands commonly form S-C structures, and wrap around feldspar porphyroclasts, which form σ-structures.

The calcsilicate Jurassic subunit has a mineral assemblage consisting of quartz, plagioclase, potassium feldspar, epidote, minor diopside ± chlorite and muscovite (Fig. 3F). This subunit is compositionally banded at millimeter- to decimeter-scales. At the grain-scale, layers of higher and lower epidote abundance within a quartz and feldspar matrix define compositional bands 1–2 mm thick. Quartz is recrystallized to approximately equigranular (~0.1 mm) subgrain aggregates and feldspars show sweeping undulose extinction and minor subgrain development. Epidote-rich bands contain 0.1–1 mm long, elongate clusters of small (<0.01 mm) grains with the long axis of the cluster parallel to the foliation.

3.2. Veins in the Saddlebag Lake Shear Zone

Veins are common within all Mesozoic units affected by the SLSZ. In most exposures, the veins occur in two sets: one discordant to the shear zone foliation and one parallel to sub-parallel to the foliation (e.g. Fig. 4).

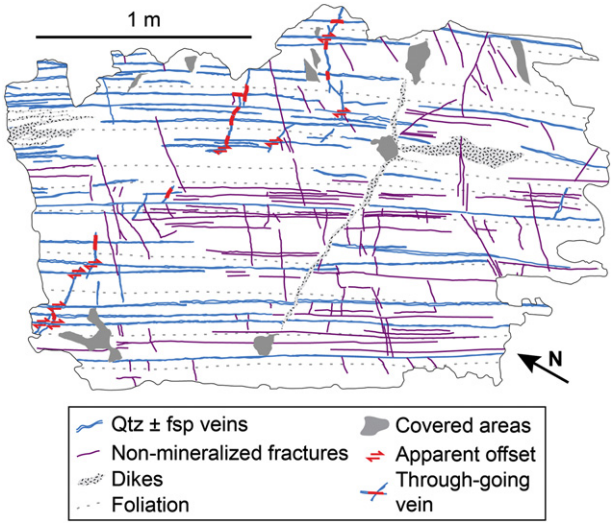

Fig. 4. Outcrop map showing an example of the distribution of foliation sub-parallel veins in the Jurassic silicate subunit. Arrows show locations where shear offsets were identified across quartz veins and thick bars show truncation relation (bar indicates through-going structure).

Discordant veins are commonly folded, but many are relatively straight. Folds in discordant veins range from tight to open with wavelengths typically <10 cm and axial traces which are locally sub-parallel to the foliation. No shear offsets were observed across veins in this set. Veins in this set are all 1–20 mm thick and contain quartz, tourmaline, tourmaline and quartz, plagioclase and quartz, or epidote. Some tourmaline veins are surrounded by a halo of lighter colored rock. Thicker tourmaline veins may also contain quartz lenses folded with the vein. Numerous epidote veins that cut all other vein compositions branch from the brittle faults, and are interpreted to have formed late in the deformation history of the system. Leucogranite dikes a few millimeters to several meters thick are found throughout the area. Some dikes are at high angle to the foliation, and may crosscut veins, but some are intruded along the foliation (e.g. Fig. 4), in which case they form interconnected arrays. Many dikes are also folded.

Foliation sub-parallel veins are straight, weakly to moderately boudinaged in both horizontal and vertical exposures (Fig. 3B), and are folded with the foliation to form open folds with axial traces at high angles to the foliation (Fig. 5). These veins are most common in the Jurassic silicate subunit, but also occur in the Triassic metavolcanics. They tend to be thin (2–4 mm on average) and predominantly contain coarse-grained, transparent to white quartz, with some veins containing quartz and plagioclase. Lengths of 45 measured foliation sub-parallel veins range from 0.4 to 4.8 m, but the majority of veins extended beyond the length of an exposure so these are minimum bounds on the true lengths. There is an average 5° local misorientation between the foliation and vein orientations in the foliation sub-parallel set. The foliation sub-parallel veins are often separated by <1 m perpendicular to vein strike, and in some areas they are spaced every ~0.01 m (Figs. 3 & 4). All of the veins in the foliation sub-parallel set are locally parallel but non-coplanar so do not connect.

Veins in the calc-silicate subunit predominantly contain quartz and are strongly boudinaged and extensively folded, commonly with isoclinal folds and occasionally refolded folds (Fig. 5). The maximum lengths of vein segments are of the order of tens of centimeters. Veins in this subunit are much less common than in the silicate-rich unit.

Some of the foliation sub-parallel veins in the Triassic and Jurassic units display measurable apparent shear offsets (Fig. 6). Structures that provide kinematic evidence for shear include offset veins, rhombochasm structures, occasional wing cracks (Cruikshank et al., 1991), and slickenline lineations on vein edges. Crosscutting relations with veins at high angles to the foliation show that the foliation sub-parallel veins both offset the high angle veins and are crosscut by them (Fig. 6). Apparent dextral shear offsets along foliation-parallel veins ranged from 2 to 63 mm, with an average apparent offset of 12 mm ($n = 60$).

Microstructures of foliation sub-parallel veins viewed perpendicular to the foliation and parallel to the lineation fall into four groups (Fig. 7) defined by quartz textures, grain shapes, and dynamic recrystallization mechanisms:

(1) Quartz grains are subhedral and elongate (grain sizes ranges from ~0.05 mm to several millimeters) with grains exhibiting undulose or patchy extinction (Fig. 7A). The long axes of elongate grains are typically at 40° angle to the vein boundaries. Small (tens of μm), rounded grains line the edges of larger grains in a core-and-mantle structure. Core grains have serrated boundaries that display bulges of similar dimension to the mantle grains. This group shows characteristics similar to Regime 1 of Hirth and Tullis (1992), where dynamic recrystallization occurs by grain boundary migration, or bulging recrystallization (BLG) (Passchier and Trouw, 2005).

(2) Quartz grains exhibit a hybrid interlobate- amoeboid texture. Small, slightly elliptical recrystallized subgrains (average grain size ~0.05 mm) grouped in clusters (Fig. 7B). All grains are aligned in a preferred orientation at an acute (~20°-40°) angle

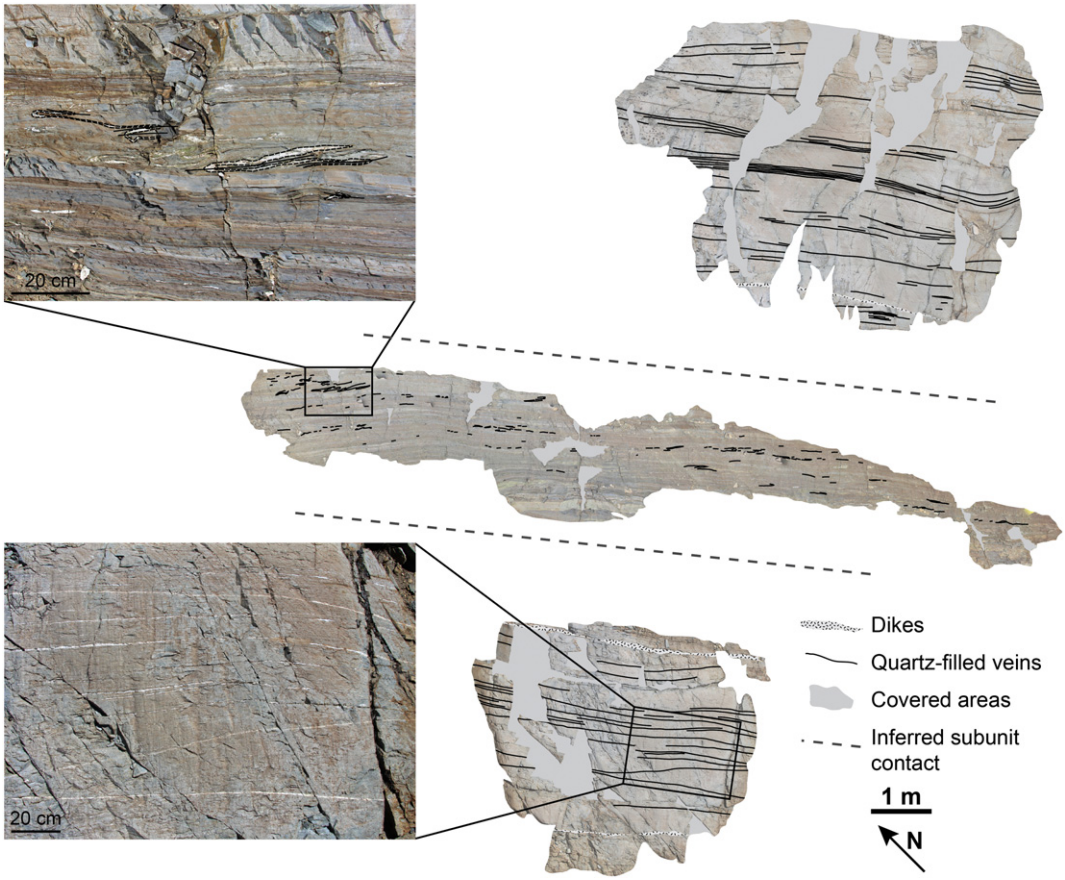

Fig. 5. Maps of three exposures illustrating the difference in the deformation of the Jurassic silicate (top and bottom panels) and calcsilicate (central panel) subunits. The exposures are shown in their correct relative positions, the areas in between were covered. The silicate subunit contains abundant, long, straight veins. The calcsilicate contains fewer, shorter, veins. Examples of isoclinally folded veins in the calcsilicate subunit are outlined with dashed lines in the upper left panel, axial traces shown by solid lines. Note the compositional banding in the calcsilicate unit.

to the vein edges. Undulose extinction is visible in larger grains, which have more elliptical shapes with aligned long axes. Aggregates of subgrains are generally separated by low angle boundaries. These characteristics are consistent with Regime 2 of Hirth and Tullis (1992) where dislocation climb is possible and dynamic recrystallization occurs by subgrain rotation (SGR).

(3) Relatively coarse quartz grains (~0.1–2 mm in diameter) with interlobate grain boundaries (Fig. 7C). Few to no subgrains are present, and extinction is uniform within the grains. Some grain boundaries form 120° triple junctions. The grains in this group are representative of grain boundary migration (GBM) recrystallization in Regime 3 of Hirth and Tullis (1992).

(4) Grains are euhedral, equigranular (grain size 0.5–0.8 mm) and polygonal (Fig. 7D). Triple-junctions are prevalent, and extinction is uniform throughout individual grains. These characteristics are representative of static recrystallization (Passchier and Trouw, 2005).

Two intermediate textures were also identified that include evidence of deformation consistent with a combination of BLG/SGR and SGR/GBM recrystallization. The former includes prevalent recrystallized grains, with the additional presence of a core-and-mantle texture and the latter contains both elongated recrystallized grains with an interlobate-amoeboid texture. Some veins exhibit equant grains with uniform extinction, lack of subgrains, and triple junction grain boundaries, suggesting these veins underwent static recrystallization. Furthermore, some of the foliation sub-parallel veins contain sub- to anhedral grains with undulose extinction and clear grain boundaries lacking an interlobate aggregate, a texture that indicates vein formation without subsequent deformation. There is no direct correlation between the microtexture of the quartz vein and distance from the pluton.

3.3. Fluid inclusion analysis

Fluid inclusions in quartz crystals within the foliation sub-parallel veins were analyzed to constrain the temperature at which the veins formed. Petrographic analysis was performed on 100 μm-thick sections oriented perpendicular to the foliation and parallel to the lineation. Fluid inclusions were studied in four samples from different locations throughout the shear zone, which represent all four microstructural groups listed above. Fluid inclusions ranged from 5 to 15 μm in diameter. Each vein analyzed contains at least one set of fluid inclusion planes, and 3 of the 4 samples contain two independent sets (Fig. 8). None of the samples contained euhedral growth shape assemblages. Set 1 is planar to slightly wavy, running parallel to sub-parallel to the orientation of the quartz vein and extending across several grain boundaries. This set has fluid inclusions scattered irregularly throughout the extent of the planes. Less than 10 planes of Set 1 were observed in any quartz vein. Set 2 contains planar arrays of fluid inclusions at an apparent angle of 80° in the plane of the section to Set 1. Set 2 planes are more abundant than Set 1, and vary in length, with some planes terminating at grain boundaries. Inclusions are evenly distributed within each plane of Set 2. No clear crosscutting relations between the two sets could be confirmed petrographically. Because the fluid inclusions are arranged in planar arrays, which cut across multiple grains and do not consistently terminate against grain boundaries or growth zones in the quartz

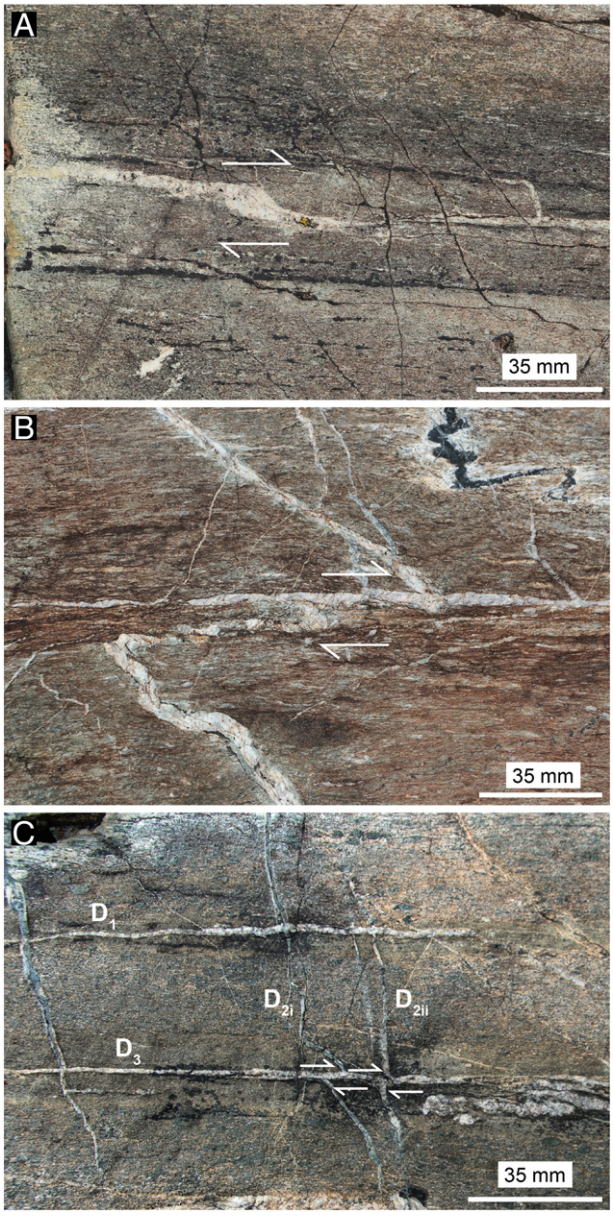

Fig. 6. A.) Apparent dextral shear offset across a foliation sub-parallel quartz veins inferred from dilational step geometry in center of the image. B.) Offset of a folded quartz vein (trending lower right to upper left in the image) by a straight foliation sub-parallel vein (horizontal, center of image). C.) Example of crosscutting relations constraining the relative timing of vein formation. Lower foliation sub-parallel vein (D_3) crosscuts two veins with apparent dextral offset (D_2), which in turn crosscut the upper foliation sub-parallel vein (D_1). Note the two D_2 veins show different amounts of apparent offset suggesting multiple increments of slip on the D_3 vein.

crystals, we interpret both sets to have formed as secondary inclusions (Roedder, 1984).

Fluid inclusion analysis was performed using a Linkam 600 heating-freezing stage attached to an Olympus BX50 petrographic microscope. Homogenization temperatures (T_h), first ice melt ($T_{eutectic}$), and final ice melt (Tm_{ice}) temperatures were measured following the method of Roedder (1984). At room temperature, both sets contain liquid rich, two-phase inclusions. The liquid phase of the inclusions appears bright in thin section, whereas the gas phase appears as dark spheres. All of the fluid inclusions homogenize exclusively into the liquid phase. No clathrate is present in the inclusions and no freezing of gas bubbles or evidence of CO_2 or CH_4 was observed, indicating that the fluid inclusions contain a binary aqueous electrolyte system containing H_2O-NaCl and that the gas bubbles contain water vapor.

Homogenization temperatures were different for Set 1 and Set 2 (Fig. 8). Average T_h of Set 1 and Set 2 were 360 °C ± 24° (1σ, $n = 38$) and 249 °C ± 16° (1σ, $n = 60$), respectively. Freezing point depressions were very similar in Set 1 and Set 2. For Set 1, the average $T_{eutectic}$ was −24.32 °C ± 1.2° (1σ, $n = 6$), and average Tm_{ice} was −1.23 °C ± 0.3° (1σ, $n = 6$), whereas for Set 2 the average $T_{eutectic}$ was −24.82 °C ± 1.2° (1σ, $n = 8$) and average Tm_{ice} was −1.47 °C ± 0.3° (1σ, $n = 6$). Microthermometry data were used to constrain the salinity, density, isochores and trapping conditions using programs included in the FLUIDS packages (Bakker, 2003). The empirical relation of Bodnar (1993) for H_2O-NaCl systems indicates salinity for Set 1 of 2.12 wt% (min = 1.62 wt%, max = 2.62 wt% based on ±1σ) and 2.52 wt% (min = 2.02 wt%, max = 3.02 wt%) for Set 2. Salinity calculations assume an isochoric inclusion to which nothing has been added post-entrapment.

Deformation of the SLSZ is interpreted to have occurred during emplacement of the Cathedral Peak pluton at ca. 86 Ma (Cao et al., 2015) and some dikes are observed to crosscut foliation sub-parallel veins (e.g. Fig. 4), so we used the pressure of crystallization of the plutons as a constraint on the pressure in the shear zone at the time the inclusions were trapped. Crystallization pressure in the TIC was between ~1.6–3 kbar (Ague and Brimhall, 1988; Memeti et al., 2009), with the Cathedral Peak and Kuna Crest granodiorites at the eastern margin of the TIC (Fig. 2) crystallizing at 1.6 kbar and 1.7 kbar respectively (Memeti et al., 2010). Based on the equations of state of Zhang and Frantz (1987), Knight and Bodnar (1989) and Bodnar and Vityk (1994) for H_2O-NaCl inclusions, the mean observed T_h and salinity for each set, with trapping pressures of 1.6 and 2.0 kbar, result in representative trapping temperatures between ~615–680 °C for Set 1 and ~380–400 °C for Set 2. As exhumation may have occurred during pluton cooling, the pluton crystallization pressure may overestimate the pressure during deformation, and these temperatures therefore likely represent upper bounds on trapping temperature.

The slightly curved shape of the Set 1 inclusion arrays may be due to folding, in which case the volume of the fluid inclusions may have been affected and the inclusions reequilibrated (i.e., changed volume, or lost/gained components). Laboratory experiments have shown that host mineral strength, fluid composition, and inclusion size and shape determine the ease of fluid inclusion reequilibration (Bodnar, 2003). The strength of quartz requires internal pressures greater >1.6 kbar to initiate reequilibration for fluid inclusions smaller than 10 μm in size (Bodnar et al., 1989). We did not observe any fractures of the host mineral locally surrounding the fluid inclusions, and the edges of inclusions themselves are regular and do not show evidence for necking. In addition, the reproducibility of homogenization temperatures, which were tested on multiple samples to ensure correct measurement, indicates that these samples have undergone minimal reequilibration (Bodnar, 2003). Because of this, observed T_h measurements for both sets of inclusions are interpreted as good constraints on the homogenization temperatures of the fluid inclusions.

Inclusions of Set 2, which form planar arrays with no indication of deformation or accompanying volume change or reequilibration, consistently indicate cooler homogenization and trapping temperatures than Set 1. A transition from predominantly plastic to entirely brittle deformation in the SLSZ (Cao et al., 2015; Hartman et al., 2015) attests to the retrograde change in temperature in the shear zone as the pluton aureole cooled. Lower homogenization temperatures in Set 2 than Set 1 are therefore consistent with a retrograde path for the SLSZ, and the associated trapping temperatures likely relate to later, cooler deformation. Set 2 trapping temperatures therefore place a lower bound on the temperature of vein formation.

4. Stable isotope geochemistry

Stable isotope analysis was performed on quartz, tourmaline and feldspar separated from the veins described above. Data from foliation

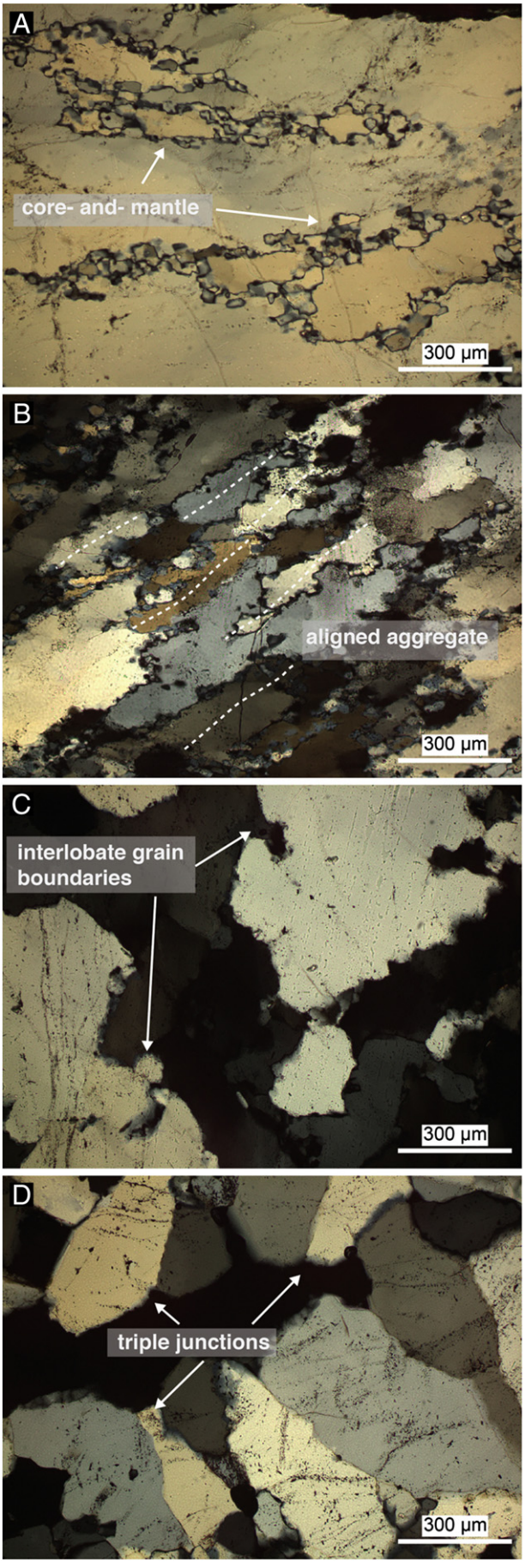

sub-parallel veins sampled throughout the study area ($n = 11$; Fig. 2) and from one exposure containing multiple generations of veins ($n = 5$; Fig. 9) constrained fluid sources. Veins were separated, crushed and sieved to 200–250 μm. Tourmaline and quartz grains were separated using a Frantz magnetic separator with 10° side tilt, 5° forward tilt, and a magnetic setting of 0.7 A. At least two to four milligrams of material were prepared for isotopic analysis. Mineral $\delta^{18}O$ and δD values were measured using the ThermoFinnigan DeltaPlusXP mass spectrometer at California State University, Long Beach (Table 1). A modified version of the laser fluorination method of Sharp (1990) was employed for the acquisition of $\delta^{18}O$ values. The TC/EA method (Sharp et al., 2001) was utilized to acquire mineral δD values. Analytical precision and accuracy for hydrogen ($\delta D = \pm 2‰$) and oxygen ($\delta^{18}O = \pm 0.2‰$) isotopes was determined using the NBS-30 biotite ($\delta D = -65.7‰$; Gröning, 2004) and Caltech Rose Quartz ($\delta^{18}O = +8.45‰$; Taylor and Epstein, 1962) standards and reported relative to V-SMOW.

In the exposure shown in Fig. 9, a large, tightly folded tourmaline vein with quartz in the center cuts the foliation and is surrounded by an alteration halo (D_1; sample KC5). Small quartz-filled fractures orthogonal to the vein edge occur at fold hinges of this vein. This tourmaline vein is cut by a ~2 mm- thick, folded quartz and plagioclase-bearing vein (D_2; sample KC2), which is apparently dextrally offset 36 mm by a few mm-thick foliation sub-parallel quartz vein (D_3; sample KC1). The D_3 foliation sub-parallel vein is crosscut by another thin, folded quartz vein (D_{4i}) and a 1 mm-wide folded quartz + tourmaline vein (D_{4ii}; sample KC3/4) without shear offset. The relative timing between the D_{4i} and D_{4ii} veins is unconstrained as they do not intersect. All veins in the outcrop are crosscut by thin, non-mineralized fractures in a variety of orientations. Fluid inclusions trapped in secondary arrays in the D_3 vein (Sets 1 and 2) constrain the temperature of fracturing and re-healing to be >400 to ~600 °C for this outcrop.

Stable isotope data from this outcrop indicate a complex fluid history. Multiple analyses of vein minerals indicate $\delta^{18}O$ heterogeneities as great as 1.7‰ at the mm-scale. Tourmaline veins (KC4, KC5) have $\delta^{18}O$ and δD values of $+7.7 \pm 0.6‰$ and $-94 \pm 1‰$, respectively (Table 1). Aqueous fluids in equilibrium (Zheng, 1993a; Jibao and Yaqian, 1997) with these veins at $T = 400–500$ °C have $\delta^{18}O = +5.8$ to $+8.2‰$ and $\delta D = -52$ to $-33‰$, values within the range of magmatic fluids (Sheppard, 1986). Though $\delta^{18}O$ and δD values of magmatic fluids and metamorphic fluids overlap, the presence of tourmaline in dikes related to the TIC and the proximal location (~390 m) of this outcrop to the plutonic complex (whole rock $\delta^{18}O = +7.5$ to $+9.0$; Kistler et al., 1986; Lackey et al., 2008) strongly suggest that waters with $\delta^{18}O$ values between +7 and +9 have a magmatic origin. Plagioclase from the folded D_2 vein (KC2) that crosscuts the older D_1 tourmaline vein (KC5) has $\delta^{18}O = +5.5 \pm 0.5‰$, a value in equilibrium (Zheng, 1993b) with magmatic fluid ($\delta^{18}O = +5.0$ to $+6.9$). Quartz from veins of younger age (KC1 and KC3) have $\delta^{18}O$ values ($+2.5$ to $+7.2$) in equilibrium (Zheng, 1993b) with a fluid having $\delta^{18}O = -2.0$ to $+4.2‰$, indicating meteoric-hydrothermal fluids (Sheppard, 1986). Tourmaline (KC4) and quartz (KC3) from the youngest D_{4ii} vein have $\delta^{18}O$ values in reverse order than that expected for an equilibrium system ($\delta^{18}O_{Quartz} > \delta^{18}O_{Tourmaline}$). Quartz $\delta^{18}O$ values lower than the adjacent intrusive rocks document the involvement of meteoric-hydrothermal fluids in the SLSZ.

Fig. 7. Microstructural characteristics of foliation sub-parallel quartz veins (cross-polarized light, the edges veins are horizontal in all images). A.) Group 1, consistent with bulging recrystallization (BLG). Small, recrystallized subgrains line the boundaries of large, original quartz grains. Larger grains exhibit patchy extinction. Note fluid inclusions planes are visible that cut multiple grain boundaries. B.) Group 2, representative of subgrain rotation recrystallization (SGR). Grains are more elongate and subgrains are larger. An alignment of the long axes of all grains is visible. The orientation is at an angle to the edges of the vein. C.) Group 3, consistent with grain boundary migration recrystallization (GBM). This group is defined by large, interlobate grains with little to no subgrains and uniform extinction. D.) Statically recrystallized quartz, characterized by uniform extinction, lack of subgrains, and triple junction grain boundaries.

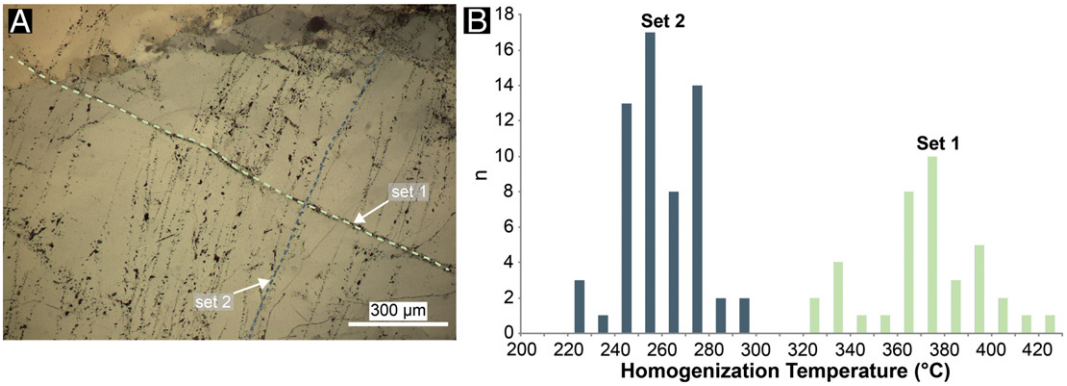

Fig. 8. A.) Photomicrograph (plane polarized light) showing the two identified sets of fluid inclusion planes. In this image, the slightly wavy Set 1 plane propagates across the entire field of view unaffected by grain boundaries (note that Set 1 is parallel to the vein margin, which is rotated away from horizontal in this view to show the quartz grain boundaries). Set 2 planes are straighter and have variable lengths, with some terminating at grain boundaries. B.) Frequency distribution of fluid inclusion homogenization temperatures showing bi-modal distribution.

Quartz and plagioclase $\delta^{18}O$ values from foliation sub-parallel veins ranged from +7.1 to +16.5‰ and +5.9‰, respectively. This wide range of $\delta^{18}O$ values indicates multiple fluid sources. Six quartz veins from the Jurassic Sawmill Canyon metasedimentary rocks have $\delta^{18}O$ values between +7.1 and +13.0. Most Sawmill Canyon samples are therefore interpreted to be in $\delta^{18}O$ equilibrium with magmatic fluids. Veins from the Triassic metavolcanic sequence mostly have higher quartz $\delta^{18}O$ values (+9.6 to +16.5; $n = 5$) than those from the Sawmill Canyon sequence, indicating magmatic and, in most cases, metamorphic fluids. The two highest $\delta^{18}O$ samples from the Triassic sequence (KC-14-29a and 30a) are the most northerly veins analyzed, potentially indicating a degree of structural segregation in the fluid flow history. One plagioclase from a Triassic sequence vein (KC-14-9a) has $\delta^{18}O$ = +5.9‰, a value in equilibrium with meteoric-hydrothermal fluid ($\delta^{18}O$ = +2.5 to +3.5‰). The stable isotope analyses of the foliation sub-parallel veins therefore show that these veins were formed from fluids of magmatic, metamorphic, and meteoric origins.

5. Discussion

5.1. Temperature and fluid conditions during vein formation

The SLSZ deformation microstructures and estimated vein formation temperatures are consistent with the range of temperatures (up to a peak around ~550–670 °C) inferred from metamorphic mineral assemblages in the contact aureole of the TIC (e.g. Kerrick, 1970). Aligned chlorite and muscovite grains define the foliation in most of the rock units we observed, reflecting deformation at low- to mid-greenschist conditions. In some cases, the platy cleavage of the chlorite grains indicates it is a retrograde pseudomorph after biotite and therefore the foliation formed at temperatures above ~400 °C. Fluid inclusion homogenization temperatures in the foliation sub-parallel quartz veins place a minimum bound on the temperature of vein formation (~250 °C for Set 2 and ~360 °C for Set 1). Trapping temperatures are higher, and suggest vein formation could have occurred at temperatures >600 °C. The trapping temperatures are relatively uncertain because the pluton crystallization pressure is not a direct constraint on the pressure during deformation, but assuming constant volume for the fluid inclusions and a retrograde thermal history, the trapping temperatures are consistent with vein formation at temperatures of >400 to ~600 °C.

The microstructural evidence for three dynamic recrystallization mechanisms in the foliation sub-parallel quartz veins is consistent with a temperature range of 300 to >500 °C during deformation following vein formation (Stipp et al., 2002). However, in addition to temperature, rates of recovery are also affected by factors such as strain rate and the presence of water (e.g. Law, 2014). The addition of trace amounts of water can decrease the temperature required for deformation by ~100 °C (Hirth and Tullis, 1992), such that quartz dynamic recrystallization microstructures can develop at lower greenschist conditions (e.g. Hirth et al., 2001). As we do not have independent constraints on strain rate or water fugacity in the Saddlebag Lake shear zone we conservatively suggest the evidence for subgrain rotation and grain boundary migration recrystallization textures reflect temperatures greater than ~400 °C. Discrete vein formation events at various distances from the pluton edge at different times during deformation in the spatio-temporal thermal field associated with pluton cooling could explain the range in quartz microstructures within the veins.

Stable isotope measurements support the presence of multiple fluid sources involved in the deformation. Tourmaline, feldspar and quartz $\delta^{18}O$ values all indicate magmatic and metamorphic fluids within the shear zone. Quartz and feldspar $\delta^{18}O$ values also record meteoric fluids, which is supported by the low fluid inclusion salinities of 2.6 wt% and 3.4 wt%. Additionally, disequilibrium in the $\delta^{18}O$ values of KC3 (quartz) and KC4 (tourmaline), which originated from the same vein, suggests a complex history that involved two independent fluid sources. Quartz lenses that post-date tourmaline with $\delta^{18}O$ values consistent with a

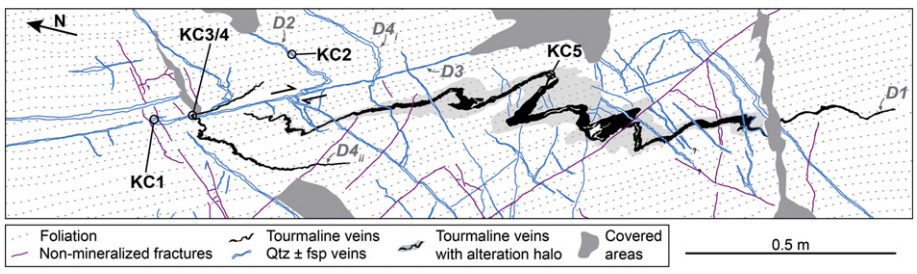

Fig. 9. Outcrop-scale map of vein deformation in the silicate-rich Jurassic unit. The relative order of vein formation of five sets of crosscutting veins is shown (D_1 to D_4). The oldest vein is the large tourmaline vein, which cuts the foliation (D_1). This vein has been transected by a series of thin quartz veins, which also cut the foliation (D_2). Shear offset of D_2 veins is seen along the foliation-parallel quartz vein (D_3). A small quartz vein (D_{4i}) cuts the foliation, crossing both D_3 and D_1 veins. A very thin, tightly folded tourmaline vein cuts D_2 veins (D_{4ii}). Red labels indicate deformation stage, blue labels refer to sample names.

Table 1
Stable isotope data from ductile-brittle veins from the Sierra Crest shear zone.

Sample	Mineral	$\delta^{18}O$	δD	Temperature	$\delta^{18}O_{water}$	δD_{water}	Fluid type
Jurassic							
KC2	Anorthite	5.2		400–500 °C	5.0 to 5.8		Magmatic
KC2	Anorthite	6.3		400–500 °C	6.1 to 6.9		Magmatic
KC2	Anorthite	5.3		400–500 °C	5.1 to 5.9		Magmatic
KC2	Anorthite	5.3		400–500 °C	5.1 to 5.9		Magmatic
KC3	Quartz	4.2		400–500 °C	−0.3 to 1.2		Meteoric-Hydr
KC3	Quartz	2.5		400–500 °C	−2.0 to −0.5		Meteoric-Hydr
KC3	Quartz	3.5		400–500 °C	−1.0 to 0.5		Meteoric-Hydr
KC4	Tourmaline	8.3	−92	400–500 °C	7.3 to 8.2	−33 to −48	Magmatic
KC4	Tourmaline	6.8	−93	400–500 °C	5.8 to 6.7	−34 to −49	Magmatic
KC4	Tourmaline	7.8		400–500 °C	6.8 to 7.7		Magmatic
KC1	Quartz	7.2		400–500 °C	2.7 to 4.2		Meteoric-Hydr
KC1	Quartz	7.1		400–500 °C	2.6 to 4.1		Meteoric-Hydr
KC5	Tourmaline	8.1	−94	400–500 °C	7.1 to 8.0	−35 to −50	Magmatic
KC5	Tourmaline	7.7	−96	400–500 °C	6.7 to 7.6	−37 to −52	Magmatic
KC-14-4a	Quartz	7.1		300–400 °C	0.1 to 2.6		Meteoric-Hydr
KC-14-14	Quartz	10.9		>500 °C	7.9 to 8.8		Magmatic
KC-14-11b	Quartz	9.4		>500 °C	6.4 to 7.3		Magmatic
KC-14-7	Quartz	13.0		300–400 °C	6.0 to 8.5		Magmatic
KC-14-5a	Quartz	12.7		300–400 °C	5.7 to 8.2		Magmatic
Triassic							
KC-14-30a	Quartz	16.5		350–450 °C	10.9 to 12.8		Metamorphic
KC-14-13a	Quartz	9.6		>450 °C	5.9 to 7.5		Magmatic
KC-14-9a	Albite	5.9		300–400 °C	2.5 to 3.5		Meteoric-Hydr
KC-14-29a	Quartz	16.3		>500 °C	13.3 to 14.2		Metamorphic
KC-14-6a	Quartz	15.1		300 to 400 °C	8.1 to 10.6		Metamorphic
KC-14-3a	Quartz	11.4		350–600 °C	5.8 to 9.3		Magmatic

Note: Fluid $\delta^{18}O$ values are calculated using the quartz-H_2O, anorthite-H_2O, and albite-H_2O fractionation factors of Zheng (1993a), and the tourmaline-H_2O fractionation factor of Zheng (1993b) at the temperatures indicated. Fluid dD values are calculated using the tourmaline-H_2O fractionation factor of Jibao and Yaqian (1997). Samples KC1 – KC5 were collected from one outcrop (Fig. 5) and are listed from youngest to oldest.

magmatic fluid origin, but which predate folding were observed in vein D_1 (Fig. 9). If the quartz in these lenses had a meteoric origin, the disequilibrium in sample KC3 could be explained by a second, later pulse of meteoric fluid that occurred after tourmaline precipitation. An alternative possible explanation for this isotopic disequilibrium is infiltration of later-stage meteoric fluids through re-opened fractures that resulted in $^{18}O/^{16}O$ exchange involving quartz but not tourmaline (e.g., LeRouge and Bouchot, 2009).

In summary, the stable isotope data are most consistent with the presence of two distinct fluids (magmatic and meteoric) that followed extended fluid-rock interaction involving metamorphic fluids. Mixed fluid systems of this kind responsible for large ore deposits are common in the vicinity of large intrusions (e.g., Bowman et al., 1987; Taylor, 1997) and major detachment fault systems (e.g., Beaudoin et al., 1992; Holk and Taylor, 2007), but the SLSZ is unusual because this hydrothermal system was centered on a strike-slip fault in the near-plutonic environment. The common characteristic of these systems is that fluid flow is driven by steep thermal gradients that existed as a neighboring plutonic complex cooled (e.g., Norton, 1984). In the case of the SLSZ, we infer that meteoric fluids infiltrated the shear zone through vertical-dominant fractures during the waning stages of cooling of the TIC.

5.2. Mechanism for shear fracture during ductile deformation

Multiple generations of veins are present in the Saddlebag Lake Shear Zone. Many veins are folded, sheared, and/or boudinaged, showing that while the bulk rock was deforming in a ductile manner, brittle structures formed and subsequently underwent ductile deformation. Furthermore, the field relationships show that brittle and ductile deformation occurred cyclically. For example, in Fig. 9, the quartz-filled shear fracture (D_3), defined by dextral offset of a folded older vein, is cut by younger quartz and tourmaline veins. These younger veins are discordant to the foliation and are folded.

Apparent shear offsets are observed across some foliation sub-parallel veins. The apertures of these veins are of the order of millimeters to centimeters, and are predominantly filled with quartz. These characteristics suggest a component of opening in addition to shear during fracture formation driven by high fluid pressure. Because no evidence of cataclastic deformation (e.g. breccia or gouge) is present along vein boundaries, and the veins contain elongate quartz aggregates at an angle to the vein margin (e.g. Fig. 7B), these fractures may have formed as fluid-assisted mixed-mode fractures (Ramsey and Chester, 2004).

The remote stress field orientation during SLSZ deformation is unknown, but veins at a high angle to the foliation that formed as mode I cracks suggest σ_1 was at a high angle to the foliation (e.g. Figs. 4 & 9). High pore pressures are typically invoked to explain slip on misoriented faults and along foliation planes in anisotropic rocks (e.g. Sibson, 1985; Sibson et al., 1988; Fagereng et al., 2010). The meteoric water source recorded in the quartz oxygen isotopes requires infiltration into the shear zone and qualitatively indicates sub-lithostatic pressure within the SLSZ, but the occurrence of pressure-driven mode I and possible mixed-mode fracture suggest that fluid pressure must have at least exceeded the least compressive stress, σ_3. Consistent with the hydrothermal mineral assemblage in the shear fractures, we infer high pore pressures contributed to the deformation. The observation that shear failure occurred along the foliation highlights the importance of mechanical anisotropy in controlling the kinematics of brittle failure in foliated rocks.

Boudinage of the foliation sub-parallel quartz veins in the SLSZ shows the foliated matrix was relatively weak compared to the quartz. Rocks containing aligned muscovite grains exhibit complex rheology, but generally support low stress at low strain rate due to a combination of grain boundary sliding and dislocation glide along basal cleavage planes in aligned grains (Mares and Kronenberg, 1993; Tullis and Wenk, 1994; Mariani et al., 2006; den Hartog et al., 2013). Pure muscovite aggregates are characterized by a friction coefficient of ~0.3 at temperatures 200–600 °C (den Hartog et al., 2013). According to the viscous flow law of Mariani et al. (2006), at 400–500 °C and a strain rate of 10^{-13} s^{-1}, a muscovite-rich rock would be very weak, supporting shear stresses of the order of 1–10 MPa. Aligned phyllosilicates also

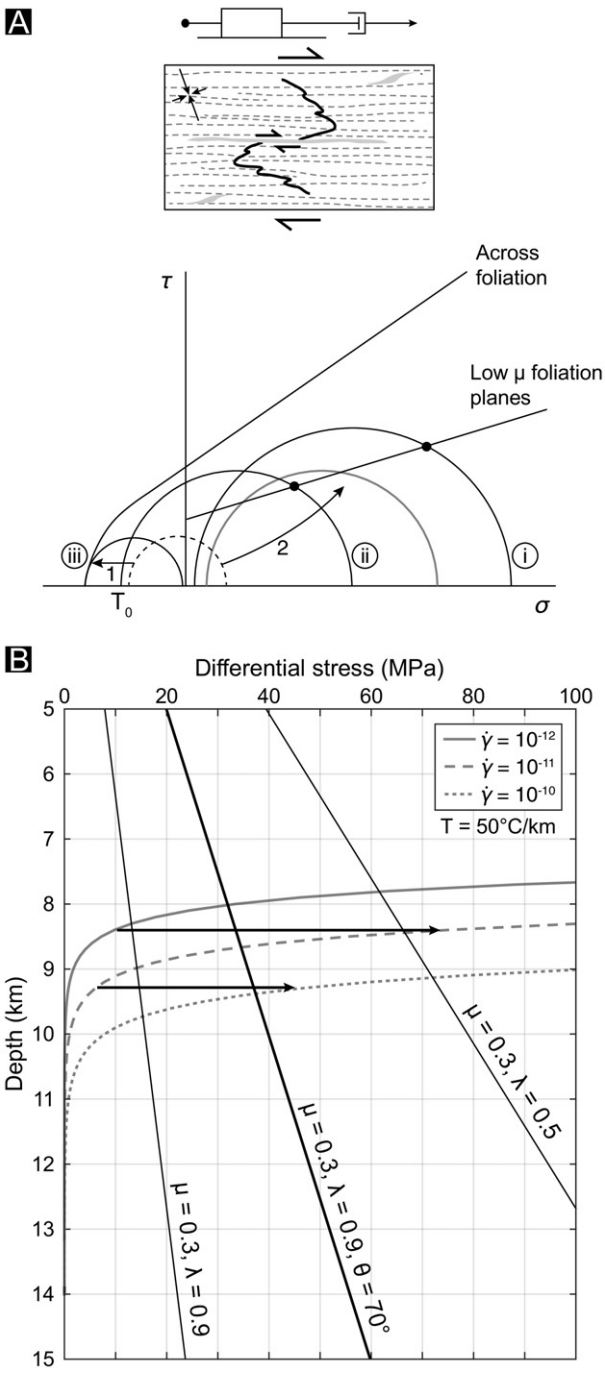

Fig. 10. Model of the formation of foliation parallel shear fractures, discordant veins, and ductile deformation under the same conditions. A.) Top: mechanical model that describes the phenomenological behavior of the system. The cartoon beneath shows a simplified representation of the main structures that formed and their orientations (possible stress field orientation indicated by arrows in the top right corner). The schematic Mohr diagram illustrates the failure, pore pressure, and loading condition scenarios that could explain the existence of mode I and II veins in the SLSZ (dots on Mohr circles represent shear stress resolved on foliation planes at high angle to σ_1). B.) Failure envelopes for frictional failure along weak foliation planes and the flow law of Mariani et al. (2006) plotted for a geothermal gradient of 50 °C/km. Close to the intersection of the frictional failure and flow law envelopes, transitional deformation is sensitive to strain rate perturbations (examples shown by arrows). See text in Section 5.2 for description.

cause rock strength in compression to vary according to the orientation of the foliation with respect to the maximum principal compressive stress, σ_1, with the lowest strength defined when the foliation is ~30° to σ_1 (e.g. Donath, 1961; Shea and Kronenberg, 1993). Interconnected bands of aligned muscovite grains are present in the foliation in the SLSZ (Fig. 3E) and minor deformation of quartz surrounding the veins in the SLSZ suggests noncoaxial deformation was partitioned into the phyllosilicates (Hunter et al., 2016). These observations suggest that viscous deformation occurred under low differential stress. However, the presence of veins within the shear zone records fracture and fluid flow, and indicates fluctuations in strain rate, stress, or pore pressure to the steady-state deformation.

Based on the field and microstructural observations, we suggest that the phenomenological behavior of the system can be described by the simple mechanical model shown in Fig. 10A, in which viscous deformation of the shear zone, represented by a dashpot, driven by a constant displacement rate across the shear zone, is connected in series with a block slider that designates fracture and frictional sliding (similar to components of the models for frictional-viscous behavior proposed by Bos and Spiers, 2002 and Niemeijer and Spiers, 2005). In this model, at low strain rates, viscous simple shear is accommodated predominantly by a combination of grain boundary sliding and dislocation migration in the phyllosilicate foliation. Low differential stress during viscous deformation is shown on the schematic Mohr diagram in Fig. 10A by the grey circle. Frictional sliding along misoriented foliation planes could be initiated by an increase in strain rate and accompanying increase in differential stress, or pore pressure (Mohr circles i and ii respectively, which intersect the Coulomb failure criterion for the foliation planes in Fig. 10A), causing the block slider to slip. A velocity-weakening behavior would result in coseismic stress drop (dashed circle). We interpret veins that cut the foliation to have formed as mode I hydrofractures at low differential stress driven by high pore pressures (Mohr circle iii). Low differential stress conditions could occur following shear fracture along foliation planes, which would transiently increase permeability, facilitating a drop in pore pressure. In this situation, hydrofracture would require relatively rapid pore pressure increase (arrow 1 in Fig. 10A) driven by cementation of the veins and continued fluid flow under a regional hydraulic gradient driven by fluid supply from the adjacent plutons. Relatively slow pore pressure build up would drive the system toward shear failure (arrow 2).

The viscous rheology of muscovite at high temperature in experiments (Mariani et al., 2006) suggests that in the transitional regime, an increase in strain rate could cause a corresponding increase in shear stress resolved on weak foliation planes sufficient to cause frictional failure. This may occur either due to a local perturbation or due to an increased displacement rate across the shear zone. Fig. 10B shows the frictional failure envelope for optimally oriented and misoriented (σ_1 at an angle, θ, of 70° to the foliation) foliation planes ($\mu = 0.3$) with the flow law for muscovite from Mariani et al. (2006). For a geothermal gradient of 50 °C/km (appropriate for the inferred temperature and depth of shear zone activity), the brittle to ductile transition occurs at ~8–10 km, consistent with the depth of crystallization of the TIC, which was syn-kinematic with ductile deformation within the SLSZ. According to the muscovite flow law, at high temperature flow stresses are so low that changes in strain rate have negligible effect on stress, but close to the transition from brittle to plastic deformation changes in strain rate have large effects on stress magnitude, which are especially significant under high pore pressure conditions (examples shown by arrows in Fig. 10B). Transitional deformation in the SLSZ may therefore be defined as deformation susceptible to switches between brittle and plastic deformation due to strain rate or pore pressure perturbations. This may be particularly important for muscovite-dominated foliations as muscovite shear zones are strain hardening at high strain rates in experiments (Mariani et al., 2006).

Multiple, crosscutting veins from the two observed vein sets in a single exposure indicate that the stress and/or pore pressure conditions changed temporally at a local scale because conditions for both foliation sub-parallel shear fracture and mode I fracture across the foliation were met. This required that differential stress decreased for mode I fracture, and subsequently recovered for shear fracture. Fluctuations in pore

pressure are also required by the observations: the pore pressure was relatively large compared to σ_3 for tensile failure, and relatively small for shear failure. Pore pressure in the SLSZ may have fluctuated due to pulses of activity in the adjacent plutons that could have transiently changed the stress, temperature, and pore pressure fields, and it must have been moderated by the fracturing/healing cycles evident within the shear zone. We suggest that the mode of fracturing and local behavior of the system was controlled by the competition between the loading rate and pore pressure build up. As the fine-grained metamorphic host rock likely had low permeability, the fracture permeability would have dominated over short timescales following fracture formation, so cementation and sealing of veins would have been a primary control on pressure fluctuations. The large number of veins in many exposures suggests that the stress – pore pressure cycling described above occurred repeatedly, and that the stress state deviated by small amounts from the steady state conditions during ductile flow within the shear zone.

Ductile deformation caused more intense folding in the Jurassic calcsilicate subunits than the silicate subunits, indicating that the calcsilicates were less competent and underwent greater non-coaxial deformation. Foliation sub-parallel veins are more common, longer and straighter in the silicate units. As the silicate units were more competent at in-situ conditions, a larger differential stress would be required to cause them to deform plastically, suggesting the high differential stress conditions were met more readily in the competent units. Heterogeneity in the rock type at meters to tens of meters scale therefore controlled the occurrence and spatial distribution of shear fractures, as has been observed previously (Fagereng et al., 2014; Hayman and Lavier, 2014).

In summary, we propose that the foliation sub-parallel shear fractures formed along mechanically weak planes during viscous deformation of the SLSZ driven by perturbations to the strain rate and/or pore pressure in a low effective stress environment. Repeated fracture during viscous flow suggests both the stress and pore pressure varied. The specific stress field in the Saddlebag Lake shear zone is unknown, but the available temperature, rheology and fluid pressure constraints suggest the model is feasible (Fig. 10B), and it is consistent with previous models explaining flow and fracture (Hayman and Lavier, 2014) and rate-dependent behavior (e.g. den Hartog and Spiers, 2014).

5.3. Relevance to active systems

The tectonic setting of the SLZS, an intra-continental dextral transpressive shear zone that was active around a cooling pluton, is similar to recently identified triggered tremor locations in Japan (Chao and Obara, 2016). Triggered tremor on onshore faults in the Hokkaido, Kanto, and possibly western Kyushu regions of Japan occurs in the vicinity of active volcanoes at depths of 15–20 km (Chao and Obara, 2016). In these regions, the proximity to active volcanoes suggests active hydrothermal fluid flow, and ambient temperatures are ~450–600 °C or higher based on observed geothermal gradients (Tanaka et al., 2004), characteristics similar to the SLSZ. The depths of triggered tremor events are often poorly constrained, but triggered tremor events as shallow as 12–15 km are also observed on the San Andreas and San Jacinto faults (Gomberg et al., 2008; Peng et al., 2009; Chao et al., 2013; Wang et al., 2013). Although the inferred depth (≤10 km) of the SLSZ deformation is less than the majority of these tremor occurrences, the range of temperatures of vein formation overlapped with active transitional regimes marked by triggered tremor occurrence due to the high temperature around the cooling TIC plutons.

As with most exhumed structures, it is impossible to recover a direct record of the seismic radiation associated with fracturing. We did not observe direct evidence for seismic slip rates (Rowe and Griffith, 2015), so shear offset veins within the SLSZ may have formed as microseismic earthquakes, creep events, or low frequency events. However, the source parameters of LFEs associated with tremor swarms (e.g. Thomas et al., 2016) can be compared with geological measurements and deformation structures (e.g. Fagereng et al., 2011) to establish whether the structures are consistent with tremor-generating slip. Measured shear fracture vein lengths in the SLSZ are >0.4–4.8 m, but many veins extended under soil cover so their true lengths could not be measured. LFE rupture patch dimensions of tens of meters predicted from magnitude ~1 events with stress drops of ~10^4 Pa reported by Thomas et al. (2016) on the San Andreas fault are therefore permitted by our observations. The measured displacements on foliation sub-parallel veins range from 2 to 63 mm, with an observational cutoff at the lower end of the range. Slip during M1 LFEs is estimated to be ~0.05 mm (Thomas et al., 2016), which would be impossible to detect in the field. Some of the veins we observed slipped multiple times to accumulate the measured displacement (Fig. 6C), suggesting that the high cumulative slip is an artifact of incremental opening of a single structure. The similarity in estimated P/T conditions in the SLSZ with active triggered tremor settings in Japan and California, the inferred fluid-assisted deformation, and the structural characteristics of the SLSZ that are comparable to LFE source parameters all suggest coupled frictional viscous deformation could be relevant to understanding the tremor source in comparable active systems.

6. Conclusions

Overall, the deformation in the SLSZ provides an insight into the conditions that promote transient brittle shear failure during aseismic (viscous) deformation. Crystal plastic deformation of the mylonites formed a well-developed spaced to continuous foliation defined by aligned muscovite and chlorite. Folded and boudinaged veins inside the shear zone formed at >400–600 °C during otherwise ductile deformation. Vein attitudes and kinematics indicate that pore pressures transiently exceeded the minimum principal compressive stress. Veins sub-parallel to the foliation display apparent shear offset consistent with the shear zone kinematics. Our interpretation that fluctuations in strain rate and/or fluid pressure in a low effective stress environment promoted shear fracture along foliation planes implies that 'asperities' in these systems are planes of weakness. If tremor and slow earthquakes are representative of transitional behavior between seismic and aseismic, insights from the SLSZ could be applicable to some active regions.

Acknowledgements

Åke Fagereng and John Platt are thanked for constructive reviews that greatly improved the paper. We wish to thank Scott Paterson for introducing us to the study area and Yosemite National Park for permission to work and sample there. Thanks also to John Ridley and Jerry Magloughlin for assistance with the fluid inclusion and stable isotope analyses, Sean Hartman for providing the map in Fig. 2, and to Gus Womeldorph and Kate Shervais for assistance in the field. This paper is dedicated to the memory of Katharine Compton.

References

Ague, J.J., Brimhall, G.H., 1988. Magmatic arc asymmetry and distribution of anomalous plutonic belts in the batholiths of California: effects of assimilation, crustal thickness, and depth of crystallization. Geol. Soc. Am. Bull. 100, 912–927.

Albertz, M., 2006. Relationships between melt-induced rheological transitions and finite strain: observations from host rock pendants of the Tuolumne Intrusive Suite, Sierra Nevada, California. J. Struct. Geol. 28, 1422–1444.

Audet, Pascal, Bostock, Michael G., Christensen, Nikolas I., Peacock, Simon M., 2009. Seismic evidence for overpressured subducted oceanic crust and megathrust fault sealing. Nature 457 (7225), 76–78.

Bakker, R.J., 2003. Package FLUIDS 1. Computer programs for analysis of fluid inclusion data and for modelling bulk fluid properties. Chem. Geol. 194 (1), 3–23.

Beaudoin, G., Taylor, B.E., Sangster, D.F., 1992. Silver-lead-zinc veins and crustal hydrology during Eocene extension, southeastern British Columbia, Canada. Geochim. Cosmochim. Acta 56, 3513–3529.

Bons, P.D., Elburg, M.A., Gomez-Rivas, E., 2012. A review of the formation of tectonic veins and their microstructures. J. Struct. Geol. 43, 33–62.

Bodnar, R.J., 1993. Revised equation and table for determining the freezing point depression of H_2O–NaCl solutions. Geochim. Cosmochim. Acta 57, 683–684.

Bodnar, R.J., 2003. Reequilibration of fluid inclusions. In: Samson, I., Anderson, A., Marshall, D. (Eds.), Fluid Inclusions: Analysis and Interpretation. Mineral. Assoc. Canada, Short Course Vol. 32, pp. 213–230.

Bodnar, R.J., Binns, P.R., Hall, D.L., 1989. Synthetic fluid inclusions. VI. Quantitative evaluation of the decrepitation behavior of fluid inclusion in quartz at one atmosphere confining pressure. J. Metamorph. Geol. 7, 229–242.

Bodnar, R.J., Vityk, M.O., 1994. Interpretation of microthermometric data for H_2O–NaCl fluid inclusions. In: de Vivo, B., Frezzotti, M.L. (Eds.), Fluid Inclusions in Minerals: Methods and Applications. Short Course IMA, pp. 117–130.

Bos, B., Spiers, C.J., 2002. Frictional-viscous flow of phyllosilicate-bearing fault rock: microphysical model and implications for crustal strength profiles. J. Geophys. Res. 107 (B2). http://dx.doi.org/10.1029/2001JB000301.

Bowman, J.R., Parry, W.T., Kropp, W.P., Kruer, S.A., 1987. Chemical and isotopic evolution of hydrothermal solutions at Bingham, Utah. Econ. Geol. 82, 395–428.

Brace, W.F., Kohlstedt, D.L., 1980. Limits on lithospheric stress imposed by laboratory experiments. J. Geophys. Res. Solid Earth 85 (B11), 6248–6252.

Brook, C.A., 1977. Stratigraphy and structure of the Saddlebag Lake roof pendant, Sierra Nevada, California. Geol. Soc. Am. Bull. 88, 321–334.

Cao, W., Paterson, S., Memeti, V., Mundil, R., Anderson, J.L., Schmidt, K., 2015. Tracking paleodeformation fields in the Mesozoic central Sierra Nevada arc: implications for intra-arc cyclic deformation and arc tempos. Lithosphere 7 (3):296–320. http://dx.doi.org/10.1130/L389.1.

Cartwright, I., Buick, I.S., 1999. The flow of surface-derived fluids through Alice Springs age middle-crustal ductile shear zones, Reynolds Range, central Australia. J. Metamorph. Geol. 17, 397–414.

Chao, K., Peng, Z., Gonzalez-Huizar, H., Aiken, C., Enescu, B., Kao, H., Velasco, A.A., Obara, K., Matsuzawa, T., 2013. A global search for triggered tremor following the 2011 Mw 9.0 Tohoku earthquake. Bull. Seismol. Soc. Am. 103 (2B), 1551–1571.

Chao, K., Obara, K., 2016. Triggered tectonic tremor in various types of fault systems of Japan following the 2012 Mw8.6 Sumatra earthquake. J. Geophys. Res. Solid Earth 121:170–187. http://dx.doi.org/10.1002/2015JB012566.

Cruikshank, K.M., Zhao, G., Johnson, A.M., 1991. Analysis of minor fractures associated with joints and faulted joints. J. Struct. Geol. 13 (8), 865–886.

den Hartog, S.A.M., Niemeijer, A.R., Spiers, C.J., 2013. Friction on subduction megathrust faults: beyond the illite–muscovite transition. Earth Planet. Sci. Lett. 373:8–19. http://dx.doi.org/10.1016/j.epsl.2013.04.036.

den Hartog, S.A.M., Spiers, C.J., 2014. A microphysical model for fault gouge friction applied to subduction megathrusts. J. Geophys. Res. Solid Earth 119:1510–1529. http://dx.doi.org/10.1002/2013JB010580.

Donath, F.A., 1961. Experimental study of shear failure in anisotropic rocks. Geol. Soc. Am. Bull. 72 (6), 985–989.

Fagereng, Å., Remitti, F., Sibson, R.H., 2010. Shear veins observed within anisotropic fabric at high angles to the maximum compressive stress. Nat. Geosci. 3 (7), 482–485.

Fagereng, Å., Remitti, F., Sibson, R.H., 2011. Incrementally developed slickenfibers—geological record of repeating low stress-drop seismic events? Tectonophysics 510 (3), 381–386.

Fagereng, Å., Hillary, G.W.B., Diener, J.F.A., 2014. Brittle-viscous deformation, slow slip, and tremor. Geophys. Res. Lett. 41:4159–4167. http://dx.doi.org/10.1002/2014GL060433.

Fisher, D.M., Brantley, S.L., 1992. Models of quartz overgrowth and vein formation: deformation and episodic fluid flow in an ancient subduction zone. J. Geophys. Res. Solid Earth 97 (B13), 20043–20061.

Gomberg, J., Rubinstein, J.L., Peng, Z., Creager, K.C., Vidale, J.E., Bodin, P., 2008. Widespread triggering of nonvolcanic tremor in California. Science 319 (5860), 173.

Greene, D.C., Schweickert, R.A., 1995. The Gem Lake shear zone: cretaceous dextral transpression in the northern Ritter Range Pendant, eastern Sierra Nevada, California. Tectonics 14, 945–961.

Gröning, M., 2004. International stable isotope reference materials. In: De Groot, P.A. (Ed.), Handbook of Stable Isotope Analytical Techniques. Vol. I. Elsevier, pp. 874–906 (Chapter 40).

Hartman, S.M., Paterson, S.R., Kirkpatrick, J.D., 2013. Transitional ductile to brittle strike-slip rheology: an exhumed laboratory of the seismogenic zone in the Eastern Central Sierra Nevada, California. Geological Society of America Annual Meeting, Denver, 2013.

Hartman, S.M., Paterson, S.R., Holk, G.J., 2015. 'An Exhumed Strike-Slip Duplex Formed at the Seismogenic Base of the Crust', Abstract T23C-2953 Presented at the Fall Meeting. AGU, San Francisco, Calif.

Hayman, N.W., Lavier, L.L., 2014. The geologic record of deep episodic tremor and slip. Geology 42 (3), 195–198.

Hirth, G., Tullis, J., 1992. Dislocation creep regimes in quartz aggregates. J. Struct. Geol. 14, 145–159.

Hirth, G., Teyssier, C., Dunlap, J.W., 2001. An evaluation of quartzite flow laws based on comparisons between experimentally and naturally deformed rocks. Int. J. Earth Sci. 90 (1), 77–87.

Hobbs, B.E., Ord, A., Teyssier, C., 1986. Earthquakes in the ductile regime? Pure Appl. Geophys. 124 (1–2), 309–336.

Holk, G.J., Taylor Jr., H.P., 2007. $^{18}O/^{16}O$ evidence for contrasting hydrothermal regimes involving magmatic and meteoric-hydrothermal waters at the Valhalla metamorphic core complex, British Columbia. Econ. Geol. 102, 1063–1078.

Horsman, E., Tikoff, B., Czeck, D., 2008. Rheological implications of heterogeneous deformation at multiple scales in the Late Cretaceous Sierra Nevada, California. Geol. Soc. Am. Bull. 120 (1–2), 238–255.

Houston, H., 2015. Low friction and fault weakening revealed by rising sensitivity of tremor to tidal stress. Nat. Geosci. 8 (5), 409–415.

Hunter, N.J., Hasalová, P., Weinberg, R.F., Wilson, C.J., 2016. Fabric controls on strain accommodation in naturally deformed mylonites: the influence of interconnected micaceous layers. J. Struct. Geol. 83, 180–193.

Jibao, G., Yaqian, Q., 1997. Hydrogen isotope fractionation and hydrogen diffusion in the tourmaline-water system. Geochim. Cosmochim. Acta 61, 4679–4688.

Johnson, K., Nissen, E., Saripalli, S., Arrowsmith, J.R., McGarey, P., Scharer, K., Blisniuk, K., 2014. Rapid mapping of ultrafine fault zone topography with structure from motion. Geosphere 10, 969–986.

Kerrich, R., 1986. Fluid infiltration into fault zones: chemical, isotopic, and mechanical effects. Pure Appl. Geophys. 124 (1–2), 225–268.

Kerrich, R., Allison, I., 1978. Vein geometry and hydrostatics during Yellowknife mineralization. Can. J. Earth Sci. 15 (10), 1653–1660.

Kerrick, D.M., 1970. Contact metamorphism in some areas of the Sierra Nevada, California. Geol. Soc. Am. Bull. 81, 2913–2938.

Kirkpatrick, J.D., Rowe, C.D., 2013. Disappearing ink: How pseudotachylytes are lost from the rock record. J. Struct. Geol. 52, 183–198.

Kistler, R., Chappell, B., Peck, D., Bateman, P.C., 1986. Isotopic variation in the Tuolumne Intrusive Suite, central Sierra Nevada, California. Contrib. Mineral. Petrol. 94, 205–220.

Knight, C.L., Bodnar, R.J., 1989. Synthetic fluid inclusions: IX. Critical PVTX properties of NaCl–H_2O solutions. Geochim. Cosmochim. Acta 53, 3–8.

Lackey, J.S., Valley, J., Chen, J., Stockli, D., 2008. Dynamic magma systems, crustal recycling, and alteration in the Central Sierra Nevada Batholith: the oxygen isotope record. J. Petrol. 49, 1397–1426.

Lavier, L.L., Bennett, R.A., Duddu, R., 2013. Creep events at the brittle ductile transition. Geochem. Geophys. Geosyst. 14:3334–3351. http://dx.doi.org/10.1002/ggge.20178.

La Rocca, M., Creager, K.C., Galluzzo, D., Malone, S., Vidale, J.E., Sweet, J.R., Wech, A.G., 2009. Cascadia tremor located near plate interface constrained by S minus P wave times. Science 323, 620–623.

Law, R.D., 2014. Deformation thermometry based on quartz c-axis fabrics and recrystallization microstructures: a review. J. Struct. Geol. 66, 129–161.

LeRouge, C., Bouchot, V., 2009. Conditions of formation and origin of fluids of quartz-tourmaline veins in the La Châtaigneraie tungstiferous district (Massif Central, France): fluid inclusions and stable isotopes. Bull. Soc. Geol. Fr. 180 (3). http://dx.doi.org/10.2113/gssgfbull.180.3.263.

Lin, A., Maruyama, T., Aaron, S., Michibayashi, K., Camacho, A., Kano, K.I., 2005. Propagation of seismic slip from brittle to ductile crust: evidence from pseudotachylyte of the Woodroffe thrust, central Australia. Tectonophysics 402 (1), 21–35.

Mares, V.M., Kronenberg, A.K., 1993. Experimental deformation of muscovite. J. Struct. Geol. 15 (9), 1061–1075.

Mariani, E., Brodie, K.H., Rutter, E.H., 2006. Experimental deformation of muscovite shear zones at high temperatures under hydrothermal conditions and the strength of phyllosilicate-bearing faults in nature. J. Struct. Geol. 28 (9), 1569–1587.

McCaig, A.M., 1988. Deep fluid circulation in fault zones. Geology 16 (10), 867–870.

McCaig, A.M., Knipe, R.J., 1990. Mass-transport mechanisms in deforming rocks: recognition, using microstructural and microchemical criteria. Geology 18 (9), 824–827.

McCaig, A.M., Wickham, S.M., Taylor, H.P., 1990. Deep fluid circulation in alpine shear zones, Pyrenees, France: field and oxygen isotope studies. Contrib. Mineral. Petrol. 106 (1), 41–60.

Melosh, B.L., Rowe, C.D., Smit, L., Groenewald, C., Lambert, C.W., Macey, P., 2014. Snap, Crackle, Pop: Dilational fault breccias record seismic slip below the brittle–plastic transition. Earth Planet. Sci. Lett. 403, 432–445.

Memeti, V., Krause, J., Anderson, J.L., Paterson, S.R., 2009. Interpreting Al-in Hornblende and Hbl-Plag thermobarometry results from the Tuolumne batholith and magmatic lobes in conjunction with single mineral element distribution electron microprobe aps. AGU Fall Meeting Abstracts Vol. 1, p. 06.

Memeti, V., Paterson, S., Matzel, J., Mundil, R., Okaya, D., 2010. Magmatic lobes as "snapshots" of magma chamber growth and evolution in large, composite batholiths: an example from the Tuolumne intrusion, Sierra Nevada, California. Geol. Soc. Am. Bull. 122 (11 − 12), 1912–1931.

Niemeijer, A.R., Spiers, C.J., 2005. Influence of phyllosilicates on fault strength in the brittle-ductile transition: insights from rock analogue experiments. Geol. Soc. Lond., Spec. Publ. 245 (1), 303–327.

Nokleberg, W.J., Kistler, R.W., 1980. Paleozoic and Mesozoic deformations in the central Sierra Nevada. U. S. Geol. Surv. Prof. Pap. 1145 (24 pp).

Norton, D.L., 1984. Theory of hydrothermal systems. Annu. Rev. Earth Planet. Sci. 12, 155–177.

Obara, K., 2002. Nonvolcanic deep tremor associated with subduction in southwest Japan. Science 296 (5573), 1679–1681.

Passchier, C.W., 1982. Pseudotachylyte and the development of ultramylonite bands in the Saint-Barthelemy Massif, French Pyrenees. J. Struct. Geol. 4 (1), 69–79.

Passchier, C.W., Trouw, R.A.J., 2005. Microtectonics. Springer Verlag, Berlin, Heidelberg (366 pp).

Paterson, S.R., Tobisch, O.T., 1992. Rates of processes in magmatic arcs: implications for the timing and nature of pluton emplacement and wall rock deformation. J. Struct. Geol. 14, 291–300.

Paterson, S.R., Žák, J., Janoušek, V., 2008. Growth of complex sheeted zones during recycling of older magmatic units into younger: Sawmill Canyon area, Tuolumne batholith, Sierra Nevada, California. J. Volcanol. Geotherm. Res. 177, 457–484.

Paterson, S.R., Memeti, V., 2014. Day 5: mesozoic volcanic rocks of the central Sierra Nevada Arc. In: Memeti, V., Paterson, S.R., Putirka, K.D. (Eds.), Formation of the Sierra Nevada Batholith: Magmatic and Tectonic Processes and Their Tempos. Society of America Field Guide Vol. 34:pp. 75–85. http://dx.doi.org/10.1130/2014.0034(05).

Peng, Z., Vidale, J.E., Wech, A.G., Nadeau, R.M., Creager, K.C., 2009. Remote triggering of tremor along the San Andreas Fault in central California. J. Geophys. Res. Solid Earth 114 (B7).

Paterson, S.R., Memeti, V., Anderson, J.L., Cao, Wenrong, Lackey, J.S., Putirka, K.D., Miller, R.B., Miller, J.S., Mundil, R., 2014. Overview of arc processes and tempos. In: Memeti, V., et al. (Eds.), Formation of the Sierra Nevada Batholith: Magmatic and Tectonic Processes and Their Tempos. Geological Society of America Field Guide Vol. 34, pp. 87–104.
Price, N.A., Johnson, S.E., Gerbi, C.C., West, D.P., 2012. Identifying deformed pseudotachylyte and its influence on the strength and evolution of a crustal shear zone at the base of the seismogenic zone. Tectonophysics 518, 63–83.
Ramsay, J.G., 1980. The crack-seal mechanism of rock deformation. Nature 284, 135–139.
Ramsey, J.M., Chester, F.M., 2004. Hybrid fracture and the transition from extension fracture to shear fracture. Nature 428 (6978), 63–66.
Roedder, E., 1984. Fluid inclusions. Rev. Mineral. 12 (644 pp).
Rowe, C.D., Griffith, W.A., 2015. Do faults preserve a record of seismic slip: a second opinion. J. Struct. Geol. 78, 1–26.
Rubinstein, J.L., Vidale, J.E., Gomberg, J., Bodin, P., Creager, K.C., Malone, S.D., 2007. Non-volcanic tremor driven by large transient shear stresses. Nature 448, 579–582.
Rubinstein, J.L., Shelly, D.R., Ellsworth, W.L., 2010. Non-volcanic tremor: a window into the roots of fault zones. In: Cloetingh, S., Negendank, J. (Eds.), New Frontiers in Integrated Solid Earth Sciences. Springer, Dordrecht, pp. 287–314.
Schweickert, R.A., Lahren, M.M., 1987. Continuation of Antler and Sonoma orogenic belts to the eastern Sierra Nevada, California, and Late Triassic thrusting in a compressional arc. Geology 15, 270–273.
Schweickert, R.A., Lahren, M.M., 2006. Geologic Evolution of Saddlebag Lake Pendant, Eastern Sierra Nevada, California: Tectonic Implications. Using Stratigraphy, Sedimentology, and Geochemistry to Unravel the Geologic History of the Southwestern Cordillera: Pacific Section, SEPM (Society for Sedimentary Geology). pp. 27–56.
Secor, D.T., 1965. Role of fluid pressure in jointing. Am. J. Sci. 263 (8), 633–646.
Sharp, Z.D., 1990. A laser-based microanalytical method for the *in situ* determination of oxygen isotope rations from silicates and oxides. Geochim. Cosmochim. Acta 54, 1353–1357.
Sharp, Z.D., Atudorei, V., Durakiewicz, T., 2001. A rapid method for determination of hydrogen and oxygen isotope ratios from water and hydrous minerals. Chem. Geol. 178, 197–210.
Shea, W.T., Kronenberg, A.K., 1993. Strength and anisotropy of foliated rocks with varied mica contents. J. Struct. Geol. 15 (9), 1097–1121.
Shelly, D.R., 2015. Complexity of the deep San Andreas Fault zone defined by cascading tremor. Nat. Geosci. 8 (2):145–151. http://dx.doi.org/10.1038/NGEO2335.
Shelly, D.R., Beroza, G.C., Ide, S., 2007. Non-volcanic tremor and low-frequency earthquake swarms. Nature 446, 305–307.
Shelly, D.R., Hardebeck, J.L., 2010. Precise tremor source locations and amplitude variations along the lower-crustal central San Andreas Fault. Geophys. Res. Lett. 37, L14301. http://dx.doi.org/10.1029/2010GL043672.
Sheppard, S.M.F., 1986. Characterization and isotopic variations in natural waters. In: Taylor, H.P., O'Neil, J.R., Valley, J.W. (Eds.), Stable Isotopes in High Temperature Systems: Reviews in Mineralogy. Vol. 16, pp. 165–183.
Sibson, R.H., Moore, J.M.M., Rankin, A.H., 1975. Seismic pumping—a hydrothermal fluid transport mechanism. J. Geol. Soc. Lond. 131 (6), 653–659.
Sibson, R.H., 1980. Transient discontinuities in ductile shear zones. J. Struct. Geol. 2 (1–2), 165–171.
Sibson, R.H., 1985. A note on fault reactivation. J. Struct. Geol. 7 (6), 751–754.
Sibson, R.H., Robert, F., Poulsen, K.H., 1988. High-angle reverse faults, fluid-pressure cycling, and mesothermal gold-quartz deposits. Geology 16 (6), 551–555.
Stevens, C.H., Greene, D.C., 1999. Stratigraphy, depositional history, and tectonic evolution of Paleozoic continental-margin rocks in roof pendants of the eastern Sierra Nevada, California. Geol. Soc. Am. Bull. 111, 919–933.
Stipp, S., Stünitz, H., Heilbronner, R., ScHmid, S.M., 2002. The eastern Tonale fault zone: a 'natural laboratory' for crystal plastic deformation of quartz over a temperature range from 250 to 700 °C. J. Struct. Geol. 24, 1861–1884.
Tanaka, A., Yamano, M., Yano, Y., Sasada, M., 2004. Geothermal gradient and heat flow data in and around Japan (I): appraisal of heat flow from geothermal gradient data. Earth Planets Space 56 (12), 1191–1194.
Taylor Jr., H.P., Epstein, S., 1962. Relationship between $^{18}O/^{16}O$ ratios in igneous and metamorphic rocks, part 1: principles and experimental results. Geol. Soc. Am. Bull. 73 (4), 461–480.
Taylor, H.P., 1997. Oxygen and hydrogen isotope relationships in hydrothermal mineral deposits. In: Barnes, H.L. (Ed.), Geochemistry of Hydrothermal Ore Deposits. Vol. 1. Wiley and Sons, CITY, p. 229.
Thomas, A.M., Nadeau, R.M., Bürgmann, R., 2009. Tremor-tide correlations and near-lithostatic pore pressure on the deep San Andreas fault. Nature 462 (7276), 1048–1051.
Thomas, A.M., Beroza, G.C., Shelly, D.R., 2016. Constraints on the source parameters of low-frequency earthquakes on the San Andreas Fault. Geophys. Res. Lett. 43: 1464–1471. http://dx.doi.org/10.1002/2015GL067173.
Tikoff, B., Teyssier, C., 1992. Crustal-scale, en echelon "P-shear" tensional bridges: a possible solution to the batholithic room problem. Geology 20 (10), 927–930.
Tikoff, B., Greene, D., 1997. Stretching lineations in transpressional shear zones: an example from the Sierra Nevada Batholith, California. J. Struct. Geol. 19, 29–39.
Tikoff, B., de Saint Blanquat, M., 1997. Transpressional shearing and strike-slip partitioning in the Late Cretaceous Sierra Nevada magmatic arc, California. Tectonics 16 (3), 442–459.
Tobisch, O.T., Saleeby, J.B., Renne, P.R., McNulty, B., Tong, W.X., 1995. Variations in deformation fields during development of a large-volume magmatic arc, Central Sierra-Nevada, California. Geol. Soc. Am. Bull. 107 (2), 148–166.
Tullis, J., Wenk, H.R., 1994. Effect of muscovite on the strength and lattice preferred orientations of experimentally deformed quartz aggregates. Mater. Sci. Eng. A 175 (1), 209–220.
Wang, T.H., Cochran, E.S., Agnew, D., Oglesby, D.D., 2013. Infrequent triggering of tremor along the San Jacinto fault near Anza, California. Bull. Seismol. Soc. Am. 103 (4), 2482–2497.
Wech, A.G., Boese, C.M., Stern, T.A., Townend, J., 2012. Tectonic tremor and deep slow slip on the Alpine Fault. Geophys. Res. Lett. 39, L10303. http://dx.doi.org/10.1029/2012GL051751.
Williams, C.F., Grubb, F.V., Galanis Jr., S.P., 2004. Heat flow in the SAFOD pilot hole and implications for the strength of the San Andreas fault. Geophys. Res. Lett. 31, L15S14. http://dx.doi.org/10.1029/2003GL019352.
Zhang, Y.G., Frantz, J.D., 1987. Determination of the homogenization temperatures and densities of supercritical fluids in the system NaCl–KCl–$CaCl_2$–H_2O using synthetic fluid inclusions. Chem. Geol. 64, 335–350.
Zheng, Y.F., 1993a. Calculation of oxygen isotope fractionation in hydroxyl-bearing silicates. Earth Planet. Sci. Lett. 120, 247–263.
Zheng, Y.F., 1993b. Calculation of oxygen isotope fractionation in anhydrous silicate minerals. Geochim. Cosmochim. Acta 57, 1079–1091.